Genesis and evolution of large-scale sediment waves in submarine canyons since the Penultimate Glacial Maximum (ca. 140 ka), northern South China Sea margin

Wei Zhou[1,2,*], Domenico Chiarella[3], Haiteng Zhuo[4], Yingmin Wang[5], Wu Tang[6], Mengjun Zou[6], Qiang Xu[6]

[1] *College of Energy, Chengdu University of Technology, Chengdu 610059, China*

[2] *State Key Laboratory of Oil and Gas Reservoir Geology and Exploitation (Chengdu University of Technology), Chengdu 610059, China*

[3] *Clastic Sedimentology Investigation (CSI) - Department of Earth Sciences, Royal Holloway University of London, Egham, Surrey TW20 0EX, UK*

[4] *School of Marine Sciences, Sun Yat-sen University, Zhuhai 519082, China*

[5] *Ocean College, Zhejiang University, Zhoushan 316021, China*

[6] *CNOOC Research Institute Co., Ltd, Beijing 100028, China*

Abstract: Sediment waves are common on the seafloor, but large-scale ones developed in submarine canyons are rarely reported. In this study, we document for the first time the Quaternary deep-water canyon-confined large-scale sediment waves developed on the northern South China Sea margin based on the analysis of a high-quality 3-D seismic reflection volume combined with a 2-D multichannel seismic reflection profile and three wells. Results show that the onset of these canyon-confined large-scale sediment waves can be dated back to the Penultimate Glacial Maximum (PGM≈140 ka). This was the last period for the Pearl River Delta to prograde over the shelf edge. And these sediment waves have

[*] Corresponding author. College of Energy, Chengdu University of Technology, Chengdu 610059, China.
E-mail address: wei.zhou.lemon@hotmail.com (W. Zhou).

continued to develop and migrate upslope until present. The large-scale sediment waves pertaining to the PGM have a dominant down-slope asymmetrical 2-D morphology with wavelengths of 1.059-6.090 km and wave heights of 3.3-32.5 m. The present large-scale sediment waves show an up-slope asymmetrical 2-D morphology with dimensions of 0.667-5.628 km wavelength and 2.7-14.0 m wave height, which are smaller relative to those at the PGM. Grain sizes of the sediment waves at the PGM and present are interpreted to be coarse, inferred from seismic reflection data by high amplitude reflections (HARs). After a comprehensive analysis of the types of sediment-laden flows, the sediment provenances, the seafloor topography and the features of the sediment waves, these large-scale sediment waves might be interpreted as cyclic steps generated by the down-slope flowing supercritical turbidity currents and associated internal hydraulic jumps along high gradient (approximately greater than 1.28°) canyon thalwegs characterized by numerous slope breaks. The evolution of the large-scale sediment waves from partially depositional at the PGM to erosion-dominated at the present is controlled by variations of the sediment supply and the submarine slope accommodation along the canyon thalweg, which is manifested in the co-evolution of the sediment waves with the canyon. The findings of this study tell us that in addition to axial channels and mass-transport complexes, large-scale sediment waves can also develop on the canyon floor, which helps to improve our understanding of the complex canyon processes. The 'large-scale sediment waves' described here may be a new potential deepwater-reservoir element for the deep-water hydrocarbon exploration associated with submarine canyons.

Keywords: Large-scale sediment waves; Submarine canyon; Turbidity current; Supercritical flow; Penultimate Glacial Maximum; northern South China Sea

1. Introduction

Sediment waves are widely used to describe "large-scale" (typically tens of metres to a few kilometres in wavelength and several metres in wave height), symmetrical to asymmetrical wave-like bedforms (possibly dunes, antidunes and cyclic steps) whose crests are positive relative to the surrounding seafloor area (Migeon et al., 2000; Wynn et al., 2000a, 2000b, 2002; Normark et al., 2002; Wynn and Stow, 2002; Cartigny et al., 2011; Symons et al., 2016; West et al., 2019). Over the last 10 years or so, it has been recognized that sediment waves are not just depositional, but that erosion and deposition can together in their formation (e.g., Cartigny et al., 2011; Symons et al., 2016). Sediment waves have been observed in either confined (e.g., canyons and channels) (Lewis and Pantin, 2002; Wynn et al., 2002; Smith et al., 2005; Paull et al., 2010) or unconfined settings (e.g., continental slope/rise, basin plain, channel levees and channel-lobe transition zones) (Damuth, 1979; Normark et al., 1980, 2002; Nakajima et al., 1998; Lewis and Pantin, 2002; Wynn et al., 2002; Gong et al., 2012). Depending on the processes associated with their formation, sediment waves can be divided into four different categories: 1) turbidity current related sediment waves (irrespective of grain size) (e.g., Migeon et al., 2000; Mulder and Alexander, 2001; Faugères et al., 2002; Wynn et al., 2002; Wynn and Stow, 2002; Arzola et al., 2008; Kuang et al., 2014; Normandeau et al., 2019; Maestrelli et al., 2020; Li et al., 2021); 2) bottom current related sediment waves (fine-grained ones are more common) (Lonsdale and Malfait, 1974; Flood, 1988; Flood and Shor, 1988; Wynn and Masson, 2008; Gong et al., 2012; Droghei et al., 2016; Miramontes et al., 2021); 3) hybrid turbidity flow and bottom current related sediment waves (e.g., Gong et al., 2012; Normandeau et al., 2019; Miramontes et al., 2020); and 4) soft-sediment deformation related sediment waves (i.e., wave-like slope creep bedforms) (Lee and Chough, 2001; Lee et al., 2002; Wynn and Stow, 2002).

In particular, thanks to the recent two decades of the recognition of cyclic steps and related supercritical bedforms in outcrops, seabed samplings, subsea seismic reflection data, multi-beam sonar and backscatter surveys, and numerical simulations (e.g., Fildani et al., 2006; Cartigny et al., 2011; Kostic, 2011; Fildani et al., 2013; Postma et al., 2014; Postma and Cartigny, 2014; Talling et al., 2015; Zhong et al., 2015; Carvajal et al., 2017; Covault et al., 2017; Fildani, 2017; Li and Gong, 2018; Li et al., 2020; Slootman and Cartigny, 2020; Maselli et al., 2021), the understanding of the gravity flow process and associated products is much closer to the essence, rather than remaining confined to the classical deep water fan model and related Bouma sequence (e.g., Bouma, 1962; Lowe, 1982; Mutti, 1992). The term cyclic step was first introduced by Parker (1996) to describe a bedform type that occurs in the upper flow regime. Cyclic steps are a series of bedforms (steps) that migrate slowly upstream, with each downward step (the lee side of the bedform) is manifested by a steeply descending flow that passes through a hydraulic jump and then reaccelerates on the flat stoss side (Cartigny et al., 2011). Recently, some upslope migrating sediment waves are interpreted as cyclic steps formed by supercritical flows interacting with the seafloor topography, especially in submarine canyons, channel-lobe transition zones as well as areas associated with flows stripped from the main meandering deep-water turbidity channel over the levee (Fildani et al., 2006; Cartigny et al., 2011; Covault et al., 2017; Li and Gong, 2018). Although small-scale (a few metres to a few hundred metres in wavelength) wave-like or crescent-shaped bedforms in these settings have been extensively reported, the large-scale ones (wavelengths of a few hundred metres to a few kilometres), particularly those developed in canyons, remain rare (Symons et al., 2016).

Large-scale sediment waves are common on the continental slope of the northern South China Sea (SCS), such as the eastern slope offshore Dongsha Islands (Kuang et al., 2014), the SCS Slope off southwestern Taiwan (Damuth 1979; Gong et al., 2012; Li et al., 2021), the Shenhu area (Li et al. 2013; Wang et al., 2018), the Xisha Trough (Chen et al., 2016), and the SCS slope off southeastern Hainan

Island (Chen et al., 2017). However, these sediment waves are all developed in an unconfined environment, and they form either independently from alongslope flowing bottom currents or downslope flowing turbidity currents, or as a product of the interaction of these two types of flow. In this study, we report for the first time the development of the Quaternary canyon-confined large-scale sediment waves (~0.7-7 km wavelength, 2.7-32.5 m wave height) along steep canyon thalwegs from the northern SCS margin, based upon high-quality, three-dimensional (3-D) seismic reflection data combined with wells and a two-dimensional (2-D) multichannel seismic reflection profile. The aims of this study are as follows: 1) to ascertain the development age of these canyon-confined large-scale sediment waves; 2) to describe the geometrical and lithological characteristics of these sediment waves; 3) to analyze the genesis of these sediment waves; (4) to study and discuss the relationship between the development of large-scale sediment waves and the evolution of submarine canyons; and 5) to point out the significance of the canyon-confined large-scale sediment waves in academia and industry.

2. Geological background

The studied area is located in the Baiyun Sag (BYS) of the Pearl River Mouth Basin (PRMB) along the northern SCS margin (Fig. 1). The SCS is a marginal sea of the west Pacific Ocean. Its abyssal basin consists of three subbasins, respectively are the East Subbasin, the Northwest Subbasin and the Southwest Subbasin. The onset of the seafloor spreading of the SCS happened at ca. 33 Ma in its northeastern part near Taiwan, then the seafloor spreading center jumped about 20 kilometers to the south and triggered the second episode of continental breakup of the SCS margin in its Southwest Subbasin at ca. 23.6 Ma (Li et al., 2014). The seafloor spreading of the SCS ended at ca. 16 Ma in its Southwest Subbasin and ca. 15 Ma in its East Subbasin (Li et al., 2014). The Baiyun Event occurred at ca. 23.6 Ma gave rise to a rapid tectonic subsidence for the BYS of the PRMB (Fig. 1) (Zhang et al., 2014). With this rapid subsidence, the northern shelf edge of the SCS migrated to the north of the BYS from the south of the BYS at ca. 23.3 Ma (Pang et al., 2007), and the following persistent tectonic subsidence has resulted in the sag becoming a deep-water intraslope sub-basin with a relatively steeper and more unstable upper slope since the Miocene. Afterwards, the continental slope in the BYS has been influenced by the neotectonics (i.e., the Dongsha Event) since the late Miocene (ca. 10.5 Ma) (Lüdmann and Wong, 1999).

During the Miocene-late Quaternary, several phases of the Pearl River shelf-margin delta developed as the sea level dropped close to or below the shelf edge (Lüdmann et al., 2001; Jiang et al., 2017; Lin et al., 2018; Liu et al., 2019). The ancient coarse-grained shelf-margin delta front was an important sediment supply for turbidity currents flowing downslope to erode the seafloor to form submarine canyons and channels and to deposit sediments to form submarine fans in the PRMB (Zhu et al., 2010; Zhou et al., 2015; Jiang et al., 2017; Wang et al., 2017). During the late Quaternary, four major phases of the Pearl River shelf-margin delta developed at the shelf edge of the PRMB during MIS (Marine Isotope Stage) 42, MIS 20, MIS 12 and MIS 6, respectively, with shorelines not far from the present shelf edge (Fig. 2) (Lüdmann et al., 2001; Lisiecki and Raymo, 2005; Liu et al., 2019). It is worth noting that the Penultimate Glacial Maximum (PGM ≈140 ka) within MIS 6 (Lisiecki and Raymo, 2005) was the final period for the Pearl River Delta (PRD) to prograde over the shelf break to deliver large amounts of materials to the adjacent continental slope (i.e., BYS) as the sea level dropped below the shelf edge (Figs. 1 and 2). Besides, the last Pearl River fluvial delta was confined to the inner-middle shelf during the Last Glacial Maximum (LGM) within MIS 2 (Lisiecki and Raymo, 2005), at the end of which the sea level was about 100 m above the water depth of the shelf edge, and the shoreline was approximately 100 km northwest of the shelf edge (Lambeck and Chappell, 2001; Lüdmann et al., 2001; Liu et al., 2016). Nowadays, the PRD is a bayhead delta confined to the Pearl River estuary. This study mainly focuses on the Quaternary sedimentary record with a geological time ranging from the PGM (ca. 140 ka) to the present.

3. Data and methods

The dataset used in this study consists of a high-quality, ~1800 km^2 three-dimensional (3-D) time-migrated seismic reflection volume, a two-dimensional (2-D) multichannel seismic reflection profile and three wells from the China National Offshore Oil Corporation (CNOOC) (Figs. 1, 2 and 3). The 3-D seismic volume has a bin size of 25 m (inline) ×12.5 m (crossline) with a sampling rate of 4 ms. And it is processed by zero-phase migration and has SEG (Society for Exploration Geologists) normal polarity reflection attributes. Therefore, in the seismic reflection profile, the positive reflection coefficients are shown as peak seismic reflections (black) and the negative reflection coefficients are shown as trough seismic reflections (red) (It should be noted that the 2-D multichannel seismic reflection profile screenshotted from *Geoframe* Software in Fig. 2 shows peak seismic reflections in red and trough seismic reflections in black). The seismic dominant frequency of the interval of interest (the top 200 ms time window below the modern seabed) ranges between 50.0 and 63.1 Hz. Acoustic velocities calculated from well B6 were 1480 m/s and 1700 m/s for the seawater and investigated sub-seabed intervals respectively (Fig. 3). Using the acoustic velocities and seismic dominant frequencies of these end-members, we estimate the vertical seismic resolution (defined as the tuning thickness: 0.25×seismic wavelength) to be 5.9 m at the seafloor and 6.7-8.5 m for the shallow sediments below. The horizontal seismic resolution can be considered equivalent to the line spacing of 25 m in W-E direction and 12.5 m in N-S direction. However, our ability to identify seafloor morphologies and calculate geometric parameters (e.g., wave height and wavelength) in seismic reflection profiles or plan views is defined as the detectability or visibility limit (Brown, 2004), which can fall below the tuning thickness restrict (Reijenstein et al., 2011).

We can therefore describe the geology and geometry of features smaller than the seismic tuning thickness, although the vertical resolution of the 3-D seismic reflection data is determined by the tuning thickness.

In this study, the seismic-well tie analysis of well P34 and age constrains from well ZQ3 (Feng et al., 1996; Zhuo et al., 2015; Liu et al. 2019) were used for seismic stratigraphic analysis and age constrain (Fig. 2). Subsequently, a bathymetric map of the seafloor (seismic horizon D3) with a horizontal resolution of 12.5 m×25 m, was generated by picking the first reflector from the 3-D seismic data. Based on the seismic-well tie analysis, the bottom boundary of the Quaternary (seismic horizon D1) and the corresponding interface of the PGM (seismic horizon D2) were identified on seismic reflection profiles. Depth and slope maps of D2 and D3 and isochore map of the unit bounded by D3 (top) and D2 (bottom) are presented as gridded surfaces with a horizontal resolution of 15 m×25 m.

Seismic attributes including root-mean-square (RMS) amplitude and coherence have been calculated and extracted from the seismic horizons (D1, D2 and D3). The RMS amplitude attribute, which represents the square root of the arithmetic mean of the squares of the amplitudes over a defined window interval (interface±10 ms in this study), is helpful for identifying coarse-grained facies in clastic marine environments (e.g., Catuneanu, 2006; Mayall et al., 2006; Jobe et al., 2015). For the coherence attribute, which is calculated by measuring the similarity of consecutive waveforms within a given sampling window (3×3 traces in this study), is useful for detecting lateral discontinuities in faults and stratigraphic features (e.g., Adeogba et al., 2005; Bahorich and Farmer, 1995).

4. Results

4.1 Seismic analysis and chronology

4.1.1 Seismic units

Two seismic units (SU1-SU2 from bottom to top) bounded by regional discontinuities (D1-D3) have been identified in the Quaternary shelf edge and slope sedimentary record (Liu et al., 2019) (Fig. 2). These discontinuities exhibit variable amplitude reflections with good lateral continuity and represent erosional surfaces (Fig. 2). Besides, discontinuities D2 and D3 show undulating features (Figs. 4 and 5).

SU1 is bounded by the discontinuities D1 (base) and D2 (top), with reflection terminations downlapping and onlapping D1, and toplapping and truncating D2 (Figs. 2 and 4). Seismic features of this unit vary from the proximal shelf edge to the distal continental slope. Wedge-shaped seismic reflections are visible proximally, with a sigmoid progradation reflection configuration and reflections of variable amplitude and moderate lateral continuity. These seismic facies represent shelf-margin deltas (SMDs). Four phases of shelf-margin deltas (SMD1-4) were identified in this unit. Distally, SU1 shows lentoid-shaped seismic reflections with a chaotic-subparallel reflection configuration with variable amplitude and variable lateral continuity. Among them, the chaotic and bank seismic facies represent mass transport deposits (MTDs), and the high-amplitude reflections (HARs) with good lateral continuity seismic facies represent deep-water sands (Figs. 4, 5 and 6).

SU2 is bounded by D2 at the base and D3 (seabed) at its top, with reflection terminations onlapping D2 and truncating D3 (Figs. 2 and 4). The seismic reflection characteristics of this unit also vary from proximal to distal. Proximally, SU2 shows wedge- shaped seismic reflections with a vertical aggradation reflection configuration with variable amplitude and moderate lateral continuity, which represents the deposition of slope clinoforms (Figs. 2, 4, 5 and 6). Distally, SU2 displays pod-shaped seismic reflections with a wave reflection configuration with variable amplitude and moderate lateral continuity, which are representative for undulating features along the axis of the canyon thalweg (Figs. 4 and 5).

4.1.2 Chronology

Combining the well-tie analysis of well P34 (Fig. 2) and dating data from well ZQ3 provided by

Feng et al. (1996), Zhuo et al. (2015) and Liu et al. (2019), discontinuity D1 is interpreted as the bottom boundary of the Quaternary with an age of ca. 2.58 Ma, discontinuity D2 is interpreted as the corresponding interface of the Penultimate Glacial Maximum (PGM≈140 ka) within MIS 6, and discontinuity D3 is the present seafloor. Thus, SU1 was formed during ca. 2.58 Ma-ca. 140 ka, and SU2 was formed during ca. 140 ka-present. Then, the undulating features confined to canyon floors in the study area were mainly formed during the period from ca. 140 ka to the present (SU2).

4.2 General seafloor morphology

At present, twenty-one straight or low sinuosity slope-confined canyons (C1-C21) form the Baiyun Slope-confined Canyon Group (BSCG), closely spaced on the upper and middle slopes of the BYS along the northern SCS margin (Fig. 1). Of these canyons, C3 and C4 show a U-shaped cross-sectional canyon morphology with wide and flat thalwegs, suggesting that these two canyons are dominated by deposition. The heads of these two canyons are closest to the shelf edge and terminal lobes are developed at the mouths of these two canyons (Fig. 1). Other canyons show a V-shaped cross-sectional canyon morphology with narrow and sharp thalwegs, which is representative of the predominance of erosion within the canyon, and they link deep-water channels at their mouths (Fig. 1). Besides, in contrast to C3, the other canyons show a series of canyon-related slope failures highlighted by the distinctive and complex seafloor topography (Fig. 3). In addition, low sinuosity axial channels are also visible to be developed in the modern thalwegs of C3, C4, C5 and C6 (Fig. 3). Of particular note is that seismic artefacts are present in the data, as imaged by the small-scale "steplike" geometry in the seismic reflections highlighted by the dip map of the seafloor and seismic reflection profiles (Figs. 3 and 4). However, they have no relationship to the ture bathymetry of the seafloor, which does not have any impact on the interpretation of large-scale features. Similar artefacts were reported by Marfurt and Alves

(2015) and Maselli et al. (2019).

At the PGM, only C3 eroded the shelf edge (Figs. 4, 5 and 6). Five slope breaks (SB*1-5*) (i.e., an abrupt decrease in slope angle) were developed along the thalweg of C3 at the PGM (Figs. 7 and 8). The longitudinal thalweg profile of C3 at the PGM is divided into two segments, respectively the upper (5.43° average slope angle) and the lower (1.28° average slope angle) segments, which are separated by one principal slope break SB1 (Fig. 7). Nine slope breaks (SB*I-IX*) are developed along the present thalweg of C3 (Figs. 7 and 8). The corresponding longitudinal thalweg profile of C3 at the present seafloor is also divided into two segments, respectively the upper (5.41° average slope angle) and the lower (1.34° average slope angle) segments which are separated by SBI (Fig. 7). In general, the lower segment of C3 at the PGM was gentler than that of the present (Fig. 7). Other canyons (C4-C6) have similar contrasting slope characteristics in areas of the undulation enrichment (Fig .5).

In addition, a series of undulations are developed along the canyons' thalwegs (Figs. 4, 5, 7 and 8). We consider them to be large-scale sediment waves rather than scours, based on the following three evidences: (1) these undulations have wavelengths significantly greater than 300 m (Figs. 4, 5 and 8) (Symons et al., 2016); (2) these undulations all have their wave crests be positive relative to the surrounding region of seafloor (Figs. 4, 5, 7 and 8), and (3) the non-isolated depressions or depocenters associated with these undulations shown by the isochore map of SU2 (Fig. 9). Because scours are predominantly erosional bedforms characterized by enclosed depressions, which cut into and lie below the surrounding region of seafloor (Symons et al., 2016, Li and Gong, 2018; Li et al., 2020).

4.3 Characteristics of the canyon-confined large-scale sediment waves

4.3.1 Canyon-confined large-scale sediment waves on the PGM seafloor

Seismic feature and geometry

In this study, we define a submarine sediment wave bedform in a seismic reflection profile as a complete wave-like feature from one wave crest, through a wave trough, to another wave crest and whose crest must be positive relative to the surrounding seafloor area (Symons et al., 2016). Seismic features of the sediment wave bedform at the PGM are represented by wave-shaped seismic reflections with variable amplitude and good continuity (Figs. 4 and 5). On the bathymetric map, the sediment waves show a regular variation in bathymetric contour spacing, i.e., contour spacing is denser and then sparser from one wave crest to another along the downslope direction, because changes in topographic slope correspond to the changes in contour spacing (Fig. 8). At the PGM, fourteen large-scale sediment waves (C3-W*a*-*d*, C4-W*a*-*d*, C5-W*a*-*d*, C6-W*a*-*b*) confined to the canyon thalwegs were identified on the basis of seismic reflection profiles combined with the bathymetric and slope maps (Figs. 4, 5 and 8). These sediment waves at the PGM have wavelengths of 1.059-6.090 km (2.316 km on average), wave heights of 3.3-32.5 m (10.0 m on average) (Table 1). Of the 14 sediment waves, 10 are displayed as a down-slope asymmetrical 2-D morphology and the others show an up-slope asymmetrical 2-D morphology (Table 1; Figs. 4 and 5).

Lithology

The stoss side of the sediment wave displays strip-like high amplitude reflections (HARs), while the lee side of the sediment wave shows weak amplitude reflections (WARs) (Figs. 4, 5 and 10A). These seismic features suggest that sand-rich sediments are mainly deposited on the stoss side of the sediment wave while mud-rich sediments are deposited on its lee side. Besides, the canyon thalweg shows low coherence seismic attributes (Fig. 10D), suggesting that the thalweg of C3 at the PGM was not dominated by the deposition of MTDs generated by mass wasting processes along the canyon axis.

Distribution

From the seismic reflection profiles and bathymetry map of the paleo-seafloor, it appears that these sediment waves were mainly developed in the middle and lower reaches of the canyons along the canyon thalwegs, with their wave crest lines parallel to the seafloor bathymetries (Figs., 4, 5 and 8). The lateral extension of the sediment waves is limited by the canyon walls (Figs. 8).

4.3.2 Canyon-confined large-scale sediment waves on the present seafloor

Seismic feature and geometry

Similar to the sediment waves identified on D2, seismic features of the sediment wave bedforms on the present seafloor (D3) are also represented by wave-shaped seismic reflections with good continuity, but high amplitudes (Figs. 4, 5 and 10). Twenty large-scale sediment waves are identified along the thalwegs of canyons on the present seafloor (C3-W*1-9*, C4-W*1-4*, C5-W*1-5*, C6-W*1-2*) (Figs, 4, 5 and 8). These sediment waves have wavelengths of 0.667-5.628 km (1.866 km on average), wave heights of 2.7-14.0 m (5.3 m on average) (Table 1). Compared to the sediment waves formed at the PGM, the current sediment waves have smaller wavelengths and wave heights, but their angle parameters are larger (Table 1). In seismic profiles, all of these twenty sediment waves display an up-slope asymmetrical 2-D morphology (Table 1; Figs. 4 and 5).

Lithology

Both sides (stoss and lee sides) of the sediment waves along the canyon thalweg at the present show strip-like HARs (Fig. 10C), indicating that sandy sediments are deposited in canyon thalwegs whether or not they are controlled by seafloor undulations. Similarly, the canyon thalweg shows low coherence seismic attributes (Fig. 10F), suggesting that the thalweg of C3 at the present is also not dominated by the deposition of MTDs generated by mass wasting processes along the canyon axis.

Distribution

Similar to the distribution of the sediment waves at the PGM, the present sediment waves also develop mainly in the middle and lower reaches of the canyons along the canyon thalwegs, with their wave crest lines parallel to the seafloor bathymetries (Figs., 4, 5 and 8). Similarly, the lateral extension of the present sediment waves is limited by the canyon walls (Figs. 3 and 8).

4.4 Evolution of the canyon-confined large-scale sediment waves

Two evolutionary stages of the canyon-confined large-scale sediment waves for both periods are identified, including the onset stage and the subsequent upslope migration stage. (1) The onset stage at the PGM. The initial development of wave-like seismic reflections is identified along discontinuity D2, while parallel-subparallel and chaotic seismic reflections dominate the slope segment of SU1 which is top-bounded by D2 (Figs. 4 and 5). (2) The upslope migration stage (SU2). During this stage, the large-scale sediment waves were persistently migrating up-slope in SU2, with their 2-D morphologies gradually evolved into up-slope asymmetry from dominant down-slope asymmetry, and their dimensions became smaller into the upslope direction (Figs. 4 and 5; Table 1). At the present, these sediment waves are still active. In addition, the pattern of coarse-grained deposits associated with sediment waves in the canyon has changed from intermittent banding at the PGM to continuous banding at the present, with the largest depocenter located at the middle reach of the canyon (Figs. 4, 5 and 9).

5. Discussion

5.1 Genesis of the canyon-confined large-scale sediment waves

Due to the absence of gravitational slip surfaces and the fact that the slope of the development area of the sediment waves is not over-steep, the sediment waves in this study have no evidence that they are associated with soft sediment deformation. With the exception of soft-sediment deformation related sediment waves, all other types of sediment waves are the product of the interaction of sediment-laden flows with the topography of the seabed. In order to ascertain the genesis of large-scale sediment waves that form in confined canyons, we should consider the following factors: 1) types of sediment-laden flows (i.e., down-slope turbidity flows along canyon thalwegs, persistent along-slope bottom currents across canyons, rectilinear up- and down-slope flowing tidal flows along canyon axes, internal waves, etc.); 2) sediment provenances (i.e., shallow-water *versus* deep-water); 3) the seafloor topography at local-scale and regional-scale; and 4) the sediment waves themselves (e.g., their geometries, internal structures, grain sizes and distributions).

In this study, (i) the large-scale sediment waves are confined to the canyon thalwegs with their wave crest lines oriented alongslope rather than oblique or orthogonal to the submarine bathymetry (Figs. 3, 4, 5 and 8), so they are unlikely originated from alongslope processes because the crest lines of alongslope bottom current-related sediment waves tend to be oblique or orthogonal to the bathymetry. For example, the along-slope intermediate water currents over the northern SCS slope (Zhu et al., 2010). (ii) The internal waves in the northern SCS originate in the Luzon Strait and propagate westward mainly along two pycnoclines (Hsu and Liu, 2000; Reeder et al., 2011; Alford et al., 2015; Ma et al., 2016). These two pycnoclines include the seasonal pycnocline within the shallow water mass (<220 m water depth) (Hsu and Liu, 2000; Bai et al., 2017), and the pycnocline along the interface between the shallow and intermediate water masses (~350 m water depth which is similar to that of the shelf edge) (Zhu et al., 2010; Bai et al., 2017). These two pycnoclines exist at relatively shallow water depths, so internal waves are unlikely to affect these large-scale sediment waves developed at 0.7-1.3 km water-depth (Figs. 4 and

5). In addition, the westward propagation of internal waves does not support the development of canyon-confined up-slope migrating sediment waves with crest lines oriented parallel to the bathymetry. Therefore, the influence of internal waves might be excluded from the genesis of these sediment waves. (iii) The ADCP mooring buoy at station M1 recorded near-bottom tidal currents (mainly semi-diurnal) in the thalweg of C14 at a water depth of 1089 m (Fig. 1), with velocities ranging from -40 cm/s to +40 cm/s (Wu et al., 2016). Tidal bottom currents with this range of velocities tend to form small-scale sandy bedforms (e.g., ripples), sand sheets, surface lineations and large mud waves on the seafloor (Xu et al., 2008; Stow et al., 2009). However, sediment waves identified in our study area are large-scale sandy bedforms (Figs, 4, 5, 8 and 11). It is therefore unlikely that tidal currents flowing along the axis of the canyon are a major factor in the generation of canyon-confined large-scale sediment waves.

It is considered that there are three possible interpretations of sediment waves: dunes, antidunes, and cyclic steps (Cartigny et al., 2011). Dunes are a type of bedforms that migrate down-slope. Antidunes are a type of bedforms that have a near-symmetrical 2-D waveform pattern, and they can migrate both upslope and downslope. And, cyclic steps are characterized by distinctly asymmetrical 2-D waveform pattern, and they migrate upslope. In our study, the large-scale sediment waves on the canyon floors all have a distinctly asymmetrical wave pattern and they have been continuously migrating upslope since their formation (Figs. 4, 5, 8 and Table 1). They are therefore unlikely to be dunes or antidunes.

Coarse-grained sediment waves have been reported at the proximal of deep-water turbidite systems, mainly in bypassed areas such as canyons, channels and channel-lobe transition zones (e.g., Wynn el al., 2002). Fine-grained sediment waves have also been found on the unconfined outer-levees of the deep-water turbidite channels as a result of the spillage of the fine-grained loading of turbidity currents (Lewis et al., 1998; Migeon et al., 2000; Nakajima and Satoh, 2001; Normark et al., 1980, 2002). Recently, there is a growing recognition that many of the sediment waves associated with turbidity currents are cyclic steps (Fildani et al., 2006; Kostic, 2011; Cartigny et al., 2011; Symons et al., 2016; Covault et al., 2017). Cyclic steps are long, wave-shaped, upstream migrating bedforms formed on slopes with high gradients and slope breaks that promote internal hydraulic jumping of turbidity currents (Slootman and Cartigny, 2020). Typically, steep continental slopes (>0.5°) promote supercritical currents flowing down the slope (Komar, 1971, 1975). In our study area, canyon axes with relatively high gradients (approximately greater than 1.28°) and abundant slope breaks may facilitate the formation of down-slope flowing supercritical turbidity currents and associated internal hydraulic jumps (e.g., internal hydraulic jumps occur at SB*1-5* on D2 and SB*I-IX* on D3 in Fig. 7), to form large-scale (a few hundred metres to a few kilometres in wavelength, a few metres to a few hundred metres in wave height) cyclic steps. The deep-water sands, shown as backset-bedded sets, are mainly deposited on the relatively gentle stoss side of the cyclic step whose steep lee side is dominated by the erosion of turbidity currents flowing downslope (Figs. 4, 5, and 10). This persistent differential erosion-deposition regime along the canyon thalweg promotes the development of long-term, up-slope migrating, large-scale partially depositional cyclic steps formed by turbidity currents (Slootman and Cartigny, 2020).

Canyon walls of C3 at the PGM were stable and lack slope failures, as are those of the present (Fig. 3), and the canyon fill of C3 in SU2 has predominantly parallel and filled seismic reflection characteristics in cross-sections (Fig. 12). These phenomena suggest that the sediment supply of the canyon fill is primarily from upstream rather than from the nearby canyon walls. At the PGM, the Pearl River delta prograded to the shelf edge to form a shelf-margin delta, most likely feeding abundant coarse-grained shallow-water sediments into the BYS to form a deep-water turbidity depositional system. This process is supported by the observation that the erosion of the shelf-edge delta by the canyon head, and the bypassing and deposition of deep-water sands on the canyon floor (Figs, 4, 7, 10 and 12). At present, although canyons do not erode the shelf edge, their heads erode the buried shelf-margin deltas as well as the modern submarine sand waves (Figs. 3, 4, 5 and 9) (Wang, 2000). As a result, the turbidity sands shown by HARs dominate the flat thalwag of the modern C3 (Figs. 10 and 12).

Moreover, the geometric characteristics of the sediment waves gradually change as the slope of canyon thalweg decreases downslope (Figs. 4, 5, 7 and 8; Table 1). This phenomenon is consistent with the variation in the behavior of turbidity currents flowing down a slope with different gradients, as also shown in numerical modeling simulations (Kostic, 2011; Covault et al., 2017). Furthermore, (i) the canyon head erosion at the proximal, (ii) the infill of canyon-confined large-scale sediment waves at the transition, and (iii) the developments of a channel-lobe transition zone and a terminal lobe at the canyon mouth form a laterally continuous deep-water turbidite depositional system related to the submarine canyon (Slootman and Cartigny, 2020) (Fig. 10). Hence, based on their typical geometry, distribution and migrating patterns, the large-scale sandy sediment waves identified in this study may be interpreted as cyclic steps, the formation of which is associated with the interaction of down-slope flowing supercritical turbidity currents with the longitudinally steep and laterally flat, confined canyon floor topography.

5.2 Relationship between the evolution of large-scale sediment waves and the slope-confined canyon system

The evolution of deep-water turbidite depositional systems is mainly controlled by the sediment supply and the slope accommodation (Richards et al., 1998). In submarine canyon systems, the sediment supply of deep-water turbidites is usually associated with rivers, shelf-edge deltas, shelf sands transported by ocean currents, or deep-water slope failures (e.g., Harris and Whiteway, 2011; Jobe et al., 2011; Lastras et al., 2011; Covault et al., 2011; Paull et al., 2011; Puig et al., 2017). The first three types of sediment supply primarily initiate down-slope flowing turbidity flows that erode the seafloor to form shelf-incising submarine canyons and the deposition of turbidites in their thalwags or on the unconfined seafloor beyond their downstream tails (Fisher et al., 2021). The last type of sediment supply mainly initiates the formation of slope-confined submarine canyons by backward slope failures along their heads, and the deposition of debris flow or mass-transport deposits in their thalwegs (Harris and Whiteway, 2011). These two mechanisms primarily control the formation of the two main types of submarine canyons in the world's oceans (Harris and Whiteway, 2011). In this study, after the PGM, the PRD was restricted within the inner and middle shelves, so that the shelf margin was dominated by vertical accretion and starvation deposition. In the meanwhile, the tectonic subsidence was persistent in the BYS. As a result, the upper slope gradually steepened and type of sediment supply connected to the canyon evolved from the coarse-grained shelf-edge delta at the PGM to the sandy upper slope failures thereafter (Fig. 12). As a result, the submarine canyons evolved from shelf-incising submarine canyons at the PGM to the slope-confined submarine canyons at the present.

The slope accommodation is defined by the difference between the topography of the sedimentary surface (e.g., the thalweg of canyons or channels) and the down-stream concave-up equilibrium slope profile (Prather et al., 1998; Pirmez et al., 2000; Kneller, 2003). Changes in the physical parameters of the turbidity flows will affect the equilibrium gradient (Kneller, 2003). Froude-supercritical flows flowing down the lee side are always thinner and faster, and less depositional (or more erosional) than the Froude-subcritical flows flowing over the stoss side, consequently the cyclic steps always migrate in the upstream direction (Slootman and Cartigny, 2020). In this study, the sediment waves are almost down-slope asymmetrical partially depostional cyclic steps at the PGM (Fig. 13A). The main depocenters associated with sediment waves are located at the middle reach of the canyon floor, and among which the depocenter associated with C3-Wb near to the canyon head is the largest (Figs, 9 and 13B). The turbidity currents flow down the canyon floor and deposit the largest amount of materials in the depocenter associated with C3-Wb, which tends to produce an overall steeper equilibrium slope profile along the longitudinal canyon thalweg under the action of differential erosion-filling mechanisms (Figs. 9 and 13B). In contrary, at the top of SU2 (i.e., the modern seabed), the sediment waves are almost up-slope asymmetrical transitional cyclic steps, whose formation is due to supercritical flows with higher Froude numbers (e.g., Fr >3) on a steeper slope and associated smaller slope accommodation relative to the down-slope asymmetrical cyclic steps (Cartigny et al., 2011). These cyclic steps are dominated by erosion and tend to reduce the equilibrium gradient and develop axial channels in the modern canyon thalwegs (Figs. 2, 7, 10 and 13B). The local slope accommodation associated with cyclic step is mainly found on its stoss side, which has been defined by Maselli et al. (2019) as '*Stoss-side accommodation*'. This local slope accommodation controls the deposition of turbidites on the stoss side of the cyclic step (Fig. 13). In addition, assuming all other parameters are equal, the *stoss-side accommodation* in the down-slope asymmetrical cyclic step should be greater than that in the up-slope asymmetrical cyclic step, so that this phenomenon would contribute to the evolution of the overall slightly steeper slope topography along the thalweg in the lower segment of the canyon from the PGM to the present. The evolution of the large-scale sediment waves and their holding canyons is a process which complements one another. In conclusion, the BSCG in this study is an excellent natural laboratory for the studying of the deepwater gravity flow depositional systems.

5.3 Significance of canyon-confined large-scale sediment waves

5.3.1 Academia

The process associated with submarine canyons is particularly complicated (e.g., Talling et al., 2015; Fildani, 2017; Fisher et al., 2021; Guiastrennec-Faugas et al., 2021). In the current academia, it is generally accepted that large-scale and small-scale bedforms can be developed on the canyon floor, such as small sediment waves, large sediment waves and scours (Fig.14) (Symons et al., 2016). On the modern canyon floor, small sediment waves and scours are very common (Fig. 14A and Fig. 14B). Besides bedforms, some other large morphological features are also very common on the canyon floor, such as channels (erosional, erosional/aggradational, aggradational) and mass transport complexes (MTCs) (Fig.14A). At present, attention is often focused on the deep-water channels, MTCs, scours and small sediment waves that develop within the canyon, to the exclusion of other possible large sedimentary phenomena, such as the large-scale sediment waves (Fig. 14C). The large-scale sediment waves may have a greater tendency to form in straight, U-shaped canyons, such as the canyons in our study area (Fig. 14C), and the examples from Lewis and Pantin (2002) and Wynn et al. (2002). Different features will reflect different regime of the sediment-laden flows interacting with different slope morphologies, as well as different time scales that shape them. Therefore, in order to study the canyon and its processes, it is important to identify and distinguish these morphological features of different scales. The conditions for the development of channels or large-scale sediment waves in canyons deserve further consideration.

Furthermore, apart from the present study area, only two regions in the world have reported canyon-confined large-scale sediment waves. The first area is the El Julan Channel (Wynn et al., 2002), and the other is the Southern Hikurnagi trough (Lewis and Pantin, 2002). Therefore, the canyon-confined large-scale sediment waves reported in our study complement the examples and expand the geometric distribution of large sediment waves established by Symons et al. (2016) (Fig. 11).

5.3.2 Industrial

In the deep water, the channel is very common on the submarine canyon floor, and the channels are an important deepwater-reservoir element for hydrocarbon exploration (Weimer and Slatt, 2007). However, our study might recognize a new potential deepwater-reservoir element- '*large-scale sediment* *waves*' for the deep-water hydrocarbon exploration associated with submarine canyons (Fig. 13). These turbidities associated with the large-scale sediment waves are deposited on the relative gentle stoss side of the large-scale, upslope migrating asymmetrical sediment wave (i.e., cyclic step) formed by the down-slope flowing supercritical turbidity currents and associated internal hydraulic jumps along the steep canyon thalweg (e.g., Postma and Cartigny, 2014; Maselli et al., 2019; Slootman and Cartigny, 2020). And these turbidities may differ in reservoir characteristics and distribution from the deep-water channel-related turbidities. Combined with the co-evolution of the submarine canyon, the morphology of the continental margin and the sediment supply, these turbidities can be banded along the canyon thalweg, which may be of significant exploration value when they reach a certain scale (Figs. 10 and 13).

6. Conclusions

Based on the analysis of a high-quality 3-D seismic reflection volume, combined with 2-D multichannel seismic reflection profiles and age constrained data from wells. The following conclusions can be drawn from this study:

1. For the first time, large-scale sediment waves are identified on submarine canyon floors on the continental slope of the northern South China Sea margin, whose development persists from the Penultimate Glacial Maximum (PGM≈140 ka) to the present. And from the PGM to the present, these sediment waves have continued to migrate upslope.

2. Large-scale sediment waves in the canyon thalwegs at the PGM have a dominant down-slope asymmetrical 2-D morphology with geometrical parameters of 0.789-6.090 km wavelength and 3.3-32.5 m wave height. And the large-scale sediment waves in the present canyon thalwegs all have an up-slope asymmetrical 2-D morphology with geometrical parameters of 0.667-5.628 km wavelength and 2.7-14.0 m wave height. The lithology of the PGM and present sediment waves

should be dominated by coarse-grained sediments as indicated by HARs in seismic reflection profiles and seismic attribute maps.

3. These sediment waves may be interpreted as cyclic steps generated by down-slope flowing supercritical turbidity currents and associated internal hydraulic jumps along relatively high-gradient (approximately greater than 1.28°) canyon thalwegs with numerous slope breaks.

4. The evolution of these large-scale sediment waves from the PGM to the present is controlled by the evolution of the sediment supply and variations of the submarine slope accommodation along canyon thalwegs. The development of large-scale sediment waves and canyons is a synergistic evolutionary process.

5. The significance of canyon-confined large-scale sediment waves reported in this study is to advance our understanding of the submarine canyons and their related complex processes. Besides, our study might recognize a new potential deepwater-reservoir element- '*large-scale sediment waves*' for the deep-water hydrocarbon exploration associated with submarine canyons.

Acknowledgements

We gratefully acknowledge the CNOOC Research Institute Co., Ltd for providing the seismic and well data. We thank Dr. Wei Li, Dr. Arnoud Slootman, and one other anonymous reviewer and the associate editor Dr. Andrew Green whose comments greatly improved this manuscript. This study was jointly sponsored by the National Natural Science Foundation of China (grants No. 42002125 and 41572083) and the National Basic Research Program of China (grant No. 2009CB219407).

References

Adeogba, A.A., McHargue, T.R., Graham, S.A., 2005. Transient fan architecture and depositional controls from near-surface 3-D seismic data, Niger Delta continental slope. AAPG Bulletin 89, 627-

643.

Alford, M.H., Peacock, T., MacKinnon, J.A., Nash, J.D., Buijsman, M.C., Centuroni, L.R., Chao, S.-Y., Chang, M.-H., Farmer, D.M., Fringer, O.B., Fu, K.-H., Gallacher, P.C., Graber, H.C., Helfrich, K.R., Jachec, S.M., Jackson, C.R., Klymak, J.M., Ko, D.S., Jan, S., Johnston, T.M.S., Legg, S., Lee, I.H., Lien, R.-C., Mercier, M.J., Moum, J.N., Musgrave, R., Park, J.-H., Pickering, A.I., Pinkel, R., Rainville, L., Ramp, S.R., Rudnick, D.L., Sarkar, S., Scotti, A., Simmons, H.L., St Laurent, L.C., Venayagamoorthy, S.K., Wang, Y.-H., Wang, J., Yang, Y.J., Paluszkiewicz, T., Tang, T.-Y., 2015. The formation and fate of internal waves in the South China Sea. Nature, 521, 65-69.

Arzola, R.G., Wynn, R.B., LAstras, G., Masson, D.G., Weaver, P.P.E., 2008. Sedimentary features and processes in the Nazaré and Setúbal submarine canyons, west Iberian margin. Marine Geology 250, 64-88.

Bahorich, M.S., Farmer, S.L., 1995. 3-D seismic coherency for faults and stratigraphic features. The Leading Edge 14, 1053-1058.

Bai, Y., Song, H.B., Guan, Y.X., Yang, S.X., 2017. Estimating depth of polarity conversion of shoaling internal solitary waves in the northeastern South China Sea. Continental Shelf Research 143, 9-17.

Bouma, A.H., 1962. Sedimentology of some Flysch Deposits: A Graphic Approach to Facies Interpretation. Elsevier Pub, Co.

Brown, A.R., 2004. Interpretation of Three-Dimensional Seismic Data, vol. 42. AAPG Memoir, Tulsa, Oklahoma, pp. 514.

Cartigny, M.J.B., Postma, G., van den Berg, J.H., Mastbergen, D.R., 2011. A comparative study of sediment waves and cyclic steps based on geometries, internal structures and numerical modeling. Marine Geology 280, 40-56.

Carvajal, C., Paull, C.K., Caress, D.W., Fildani, A., Lundsten, E., Anderson, K., Maier, K.L., McGann， M., Gwiazda, R., Herguera, J.C., 2017. Unraveling the channel-lobe transition zone with high-resolution AUV bathymetry: Navy Fan, offshore Baja California, Mexico. Journal of Sedimentary Research 87, 1049-1059.

Catuneanu, O., 2006. Principles of Sequence Stratigraphy. Elsevier, Amsterdam. 51-56 pp.

Chen, H.J., Zhan, W.H., Li, L.Q., Wen, M.-M., 2017. Occurrence of submarine canyons, sediment waves and mass movements along the northern continental slope of the South China Sea. Journal of Earth System Science 126, 73.

Chen, H., Xie, X.N., Zhang, W.Y., Shu, Y.Q., Wang, D.X., Vandorpe, T., Van Rooij, D., 2016. Deep-water sedimentary systems and their relationship with bottom currents at the intersection of Xisha Trough and Northwest Sub-Basin, South China Sea. Marine Geology 378, 101-113.

Covault, J.A., Kostic, S., Paull, C.K., Sylvester, Z., Fildani, A., 2017. Cyclic steps and related supercritical bedforms: Building blocks of deep-water depositional systems, western North America. Marine Geology 393, 4-20.

Covault, J.A., Romans, B.W., Graham, S.A., Fildani, A., Hilley, G.E., 2011. Terrestrial source to deep-sea sink sediment budgets at high and low sea levels: insights from tectonically active southern California. Geology 39, 619-622.

Damuth, J.E., 1979. Migrating sediment waves created by turbidity currents in the northern South China Sea Basin. Geology 7, 520-523.

Droghei, R., Falcini, F., Casalbore, D., Martorelli, E., Mosetti, R., Sannino, G., Santoleri, R., Chiocci, F.L., 2016. The role of internal solitary waves on deep-water sedimentary processes: the case of up-slope migrating sediment waves off the Messina Strait. Scientific Reports 6, 36376.

Faugères, J.-C., Gonthier, E., Mulder, T., Kenyon, N., Cirac, P., Griboulard, R., Berné, S., Lesuavé, R., 2002. Multi-process generated sediment waves on the Landes Plateau (Bay of Biscay, North Atlantic). Marine Geology 182, 279-302.

Fildani, A., 2017. Submarine canyons: A brief review looking forward. Geology 45, 383-384.

Fildani, A., Hubbard, S.M., Covault, J.A., Maier, K.L., Romans, B.W., Traer, M., Rowland, J.C., 2013. Erosion at inception of deep-sea channels. Marine and Petroleum Geology 41, 38-61.

Fildani, A., Normark, W.R., Kostic, S., Parker, G., 2006. Channel formation by flow stripping: large-scale scour features along the Monterey East Channel and their relation to sediment waves. Sedimentology 53, 1265-1287.

Fisher, W.L., Galloway, W.E., Steel, R.J., Olariu, C., Kerans, C., Mohrig, D., 2021. Deep-water depositional systems supplied by shelf-incising submarine canyons: Recognition and significance in the geologic record. Earth-Science Reviews 214, 103531.

Flood, R.D., 1988. A lee wave model for deep-sea mudwave activity. Deep-Sea Research 35, 973-983.

Flood, R.D., Shor, A.N., 1988. Mud waves in the Argentine Basin and their relationship to regional bottom circulation patterns. Deep-Sea Research 35, 943-971.

Gong, C.L., Wang, Y.M., Peng, X.C., Li, W.G., Qiu, Y., Xu, S., 2012. Sediment waves on the South China Sea Slope off southwestern Taiwan: Implications for the intrusion of the Northern Pacific Deep Water into the South China Sea. Marine and Petroleum Geology 32, 95-109.

Guiastrennec-Faugas, L., Gillet, H., Peakall, J., Dennielou, B., Gaillot, A., Jacinto, R.S., 2021. Initiation and evolution of knickpoints and their role in cut-and-fill processes in active submarine channels. Geology 49, 314-319.

Harris, P.T., Whiteway, T., 2011. Global distribution of large submarine canyons: Geomorphic differences between active and passive continental margins. Marine Geology 285, 69-86.

Hsu, M.-K., Liu, A.K., 2000. Nonlinear internal waves in the South China Sea. Canadian Journal of Remote Sensing 26, 72-81

Jiang, J., Shi, H.S., Lin, C.S., Zhang, Z.T., Wei, A., Zhang, B., Shu, L.F., Tian, H.X., Tao, Z., Liu, H.Y., 2017. Sequence architecture and depositional evolution of the Late Miocene to Quaternary northeastern shelf margin of the South China Sea. Marine and Petroleum Geology 81, 79-97.

Jobe, Z.R., Lowe, D.R., Uchytil, S.J., 2011. Two fundamentally different types of submarine canyons along the continental margin of Equatorial Guinea. Marine and Petroleum Geology 28, 843-860.

Jobe, Z.R., Sylvester, Z., Parker, A.O., Howes, N., Slowey, N., Pirmez, C., 2015. Rapid adjustment of submarine channel architecture to changes in sediment supply. Journal of Sedimentary Research 85, 729-753.

Kneller, B., 2003. The influence of flow parameters on turbidite slope channel architecture. Marine and Petroleum Geology 20, 901-910.

Komar, P.D., 1971. Hydraulic jumps in turbidity currents. Geological Society of America Bulletin 82, 1477-1488.

Komar, P.D., 1975. Supercritical flow in density currents: a discussion. Journal of Sedimentary Petrology 45, 747-749.

Kostic, S., 2011. Modeling of submarine cyclic steps: Controls on their formation, migration, and architecture. Geosphere 7, 294-304.

Kuang, Z.G., Zhong, G.F., Wang, L.L., Guo, Y.Q., 2014. Channel-related sediment waves on the eastern slope offshore Dongsha Islands, northern South China Sea. Journal of Asian Earth Sciences 79, 540-551.

Lambeck, K., Chappell, J., 2001. Sea level change through the last Glacial Cycle. Science 292, 679-686.

Lastras, G., Canals, M., Amblas, D., Lavoie, C., Church, I., Mol, B.D., Duran, R., Calafat, A.M., Hughes-Clarke, J.E., Smith, C.J., Heusner, S. and "Euroleón" cruise shipboard party, 2011. Understanding sediment dynamics of two large submarine valleys from seafloor data: Blanes and La Fonera canyons, northwestern Mediterranean Sea. Marine Geology 280, 20-39.

Lee, H.J., Syvitski, J.P.M., Parker, G., Orange, D., Locat, J., Hutton, E.W.H., Imran, J., 2002. Distinguishing sediment waves from slope failure deposits: field examples, including the 'Humboldt slide', and modelling results. Marine Geology 192, 79-104.

Lee, S.H., Chough, S.K., 2001. High-resolution (2-7 kHz) acoustic and geometric characters of submarine creep deposits in the South Korea Plateau, East Sea. Sedimentology 48, 629-644.

Lewis, K.B., Collot, J., Lallemand, S.E., 1998. The dammed Hikurangi Trough: a channel-fed trench blocked by subducting seamounts and their wake avalanches (New Zealand-France GeodyNZ project). Basin Research 10, 441-468.

Lewis, K.B., Pantin, H.M., 2002. Channel-axis, overbank and drift sediment waves in the southern Hikurangi Trough, New Zealand. Marine Geology 192, 123-151.

Li, C.-F., Xu, X., Lin, J., Sun, Z., Zhu, J., Yao, Y., Zhao, X., Liu, Q., Kulhanek, D.K., Wang, J., Song, T., Zhao, J., Qiu, N., Guan, Y., Zhou, Z., Williams, T., Bao, R., Briais, A., Brown, E.A., Chen, Y., Clift, P.D., Colwell, F.S., Dadd, K.A., Ding, W., Hernández Almeida, I., Huang, X.-L., Hyun, S., Jiang, T., Koppers, A.A.P., Li, Q., Liu, C., Liu, Z., Nagai, R.H., Peleo-Alampay, A., Su, X., Tejada, M.L.G., Trinh, H.S., Yeh, Y.-C., Zhang, C., Zhang, F., Zhang, G.-L., 2014. Ages and magnetic structures of the South China Sea constrained by deep tow magnetic surveys and IODP Expedition 349. Geochemistry, Geophysics, Geosystems 15, 4958-4983.

Li, H., Wang, Y.M., Zhu, W.L., Xu, Q., He, Y.B., Tang, W., Zhuo, H.T., Wang, D., Wu, J.P., Li, D., 2013. Seismic characteristics and processes of the Plio-Quaternary unidirectionally migrating channels and contourites in the northern slope of the South China Sea. Marine and Petroleum Geology 43, 370-380.

Li, L., Gong, C.L., 2018. Gradual transition from net erosional to net depositional cyclic steps along the submarine distributary channel thalweg in the Rio Muni Basin: A joint 3-D seismic and numerical approach. Journal of Geophysical Research: Earth Surface 123, 2087-2106.

Li, S., Li, W., Alves, T.M., Wang, J., Feng, Y., Sun, J., Li, J., Wu, S., 2020. Large-scale scours formed by supercritical turbidity currents along the full length of a submarine canyon, northeast South China Sea. Marine Geology 424, 106158.

Li, W., Li, S., Alves, T.M., Rebesco, M., Feng, Y.G., 2021. The role of sediment gravity flows on the morphological development of a large submarine canyon (Taiwan Canyon), north-east South China Sea. Sedimentology 68, 1091-1108.

Lin, C.S., Jiang, J., Shi, H.S., Zhang, Z.T., Liu, J.Y., Qin, C.G., Li, H., Ran, H.J., Wei, A., Tian, H.X, Xing, Z.C., Yao, Q.Y., 2018. Sequence architecture and depositional evolution of the northern continental slope of the South China Sea: responses to tectonic processes and changes in sea level. Basin Research 30 (Suppl. 1), 568-595.

Lisiecki, L.E., Raymo, M.E., 2005. A Pliocene-Pleistocene stack of 57 globally distributed benthic δ18O records. Paleoceanography 20, 1-17.

Liu, H.Y., Lin, C.S., Zhang, Z.T., Zhang, B., Jiang, J., Tian, H.X., Liu, H., 2019. High-resolution sequence architecture and depositional evolution of the Quaternary in the northeastern shelf margin of the South China Sea. Acta Oceanol. Sin. 38, 86-98.

Liu, J.G., Xiang, R., Kao, S.-J., Fu, S.Y., Zhou, L.P., 2016. Sedimentary responses to sea-level rise and Kuroshio Current intrusion since the Last Glacial Maximum: grain size and clay mineral evidence from the northern South China Sea slope. Palaeogeography, Palaeoclimatology, Palaeoecology 450, 111-121.

Lonsdale, P., Malfait, B., 1974. Abyssal dunes of foraminiferal sand on the Carnegie ridge. Geological Society of America Bulletin 85, 1697-1712.

Lowe, D.R., 1982. Sediment gravity flows: II. Depositional models with special reference to the deposits of high-density turbidity currents. Journal of Sedimentary Research 52, 0279-0297.

Lüdmann, T., Wong, H.K., 1999. Neotectonic regime on the passive continental margin of the northern South China Sea. Tectonophysics 311, 113-138.

Lüdmann, T., Wong, H.K., Wang, P.X., 2001. Plio-Quaternary sedimentation processes and neotectonics of the northern continental margin of the South China Sea. Marine Geology 172, 331-358.

Ma, X.C., Yan, J., Hou, Y.J., Lin, F.L., Zheng, X.F., 2016. Footprints of obliquely incident internal solitary waves and internal tides near the shelf break in the northern South China Sea. Journal of Geophysical Research: Oceans 121, 8706-8719.

Maestrelli, D., Maselli, V., Kneller, B., Chiarella, D., Scarselli, N., Vannucchi, P., Jovane, L., Iacopini, D., 2020. Characterisation of submarine depression trails driven by upslope migrating cyclic steps: Insights from the Ceará Basin (Brazil). Marine and Petroleum Geology 115, 104291.

Marfurt, K.J., Alves, T.M., 2015. Pitfalls and limitations in seismic attribute interpretation of tectonic features. Interpretation 3, SB5-SB15.

Maselli, V., Kneller, B., Taiwo, O.L., Iacopini, D., 2019. Sea floor bedforms and their influence on slope accommodation. Marine and Petroleum Geology 102, 625-637.

Maselli, V., Micallef, A., Normandeau, A., Oppo, D., Iacopini, D., Green, A., Ge, Z., 2021. Active faulting controls bedform development on a deep-water fan. Geology 49. https://doi.org/10.1130/G49206.1.

Mayall, M., Jones, E., Casey, M., 2006. Turbidite channel reservoirs-Key elements in facies prediction and effective development. Marine and Petroleum Geology 23, 821-841.

Migeon, S., Savoye, B., Faugeres, J.-C., 2000. Quaternary development of migrating sediment waves in the Var deep-sea fan: distribution, growth pattern, and implication for levee evolution. Sedimentary Geology 133, 265-293.

Miramontes, E., Eggenhuisen, J.T., Jacinto, R.S., Poneti, G., Pohl, F., Normandeau, A., Campbell, D.C., Hernández-Molina, F.J., 2020. Channel-levee evolution in combined contour current-turbidity current flows from flume-tank experiments. Geology 48, 353-357.

Miramontes, E., Thiéblemont, A., Babonneau, N., Penven, P., Raisson, F., Droz, L., Jorry, S.J., Fierens, R., Counts, J.W., Wilckens, H., Cattaneo, A., Jouet, G., 2021. Conourite and mixed turbidite-contourite systems in the Mozambique Channel (SW Indian Ocean): Link between geometry, sediment characteristics and modelled bottom currents. Marine Geology 437, 106502.

Mulder, T., Alexander, J., 2001. The physical character of subaqueous sedimentary density flows and their deposits. Sedimentology 48, 269-299.

Mutti, E., 1992. Turbidite sandstones. Parma, Italy, Universita di Parma, Istituto de Geologia, Agip, p. 275.

Nakajima, T., Satoh, M., 2001. The formation of large mudwaves by turbidity currents on the levees of the Toyama deep-sea channel, Japan Sea. Sedimentology 48, 435-463.

Normandeau, A., Campbell, D.C., Cartigny, M.J.B., 2019. The influence of turbidity currents and contour currents on the distribution of deep-water sediment waves offshore eastern Canada. Sedimentology 66, 1746-1767.

Normark, W.R., Hess, G.R., Stow, D.A.V., Bowen, A.J., 1980. Sediment waves on the Monterey Fan levee: A preliminary physical interpretation. Marine Geology 37, 1-18.

Normark, W.R., Piper, D.J.W., Posamentier, H., Pirmez, C., Migeon, S., 2002. Variability in form and growth of sediment waves on turbidite channel levees. Marine Geology 192, 23-58.

Pang, X., Chen, C., Peng, D., Zhu, M., Shu, Y., He, M., Shen, J., Liu, B., 2007. Sequence stratigraphy of deep-water fan system of Pearl River, South China Sea. Earth Science Frontiers 14, 220-229.

Parker, G., 1996. Some speculations on the relation between channel morphology and channel-scale flow structures. In: Ashworth, P., Benett, S.J., Best, J.L., McLelland, S.J. (Eds.) Coherent Flow Structures in Open Channels. Wiley, pp. 429-432.

Paull, C.K., Caress, D.W., Ussler III, W., Lundsten, E., Merner-Johnson, M., 2011. High-resolution bathymetry of the axial channels within Monterey and Soquel submarine canyons, offshore central California. Geosphere 7, 1077-1101.

Paull, C.K., Ussler III. W., Caress, D.W., Lundsten, E., Covault, J.A., Maier, K.L., Xu, J.P., Augenstein, S., 2010. Origins of large crescent-shaped bedforms within the axial channel of Monterey Canyon, offshore California. Geosphere 6, 755-774.

Pirmez, C., Beauboeuf, R.T., Friedmann, S.J., Mohrig, D.C., 2000. Equilibrium profile and baselevel in submarine channels: examples from Late Pleistocene systems and implications for the architecture of deepwater reservoirs. In: Weimer, P., Slatt, R.M., Coleman, J., Rosen, N.C., Nelson, H., Bouma, A.H., Styzen, M.J., Lawrence, D.T. (Eds.), Deep Water Reservoirs of the World. GCSSEPM Foundation, Houston, pp. 782-805.

Postma, G., Cartigny, M.J.B., 2014. Supercritical and subcritical turbidity currents and their deposits-A synthesis. Geology 42, 987-990.

Postma, G., Kleverlaan, K., Cartigny, M.J.B., 2014. Recognition of cyclic steps in sandy and gravelly turbidite sequences, and consequences for the Bouma facies model. Sedimentology 61, 2268-2290.

Prather, B.E., Booth, J.E., Steffens, G.S., Craig, P.A., 1998. Classification, lithologic calibration, and stratigraphic succession of seismic facies of intraslope basins, deep-water Gulf of Mexico. AAPG Bulletin 82, 701-728.

Puig, P., Durán,R., Muñoz, A., Elvira, E., Guillén, 2017. Submarine canyon-head morphologies and inferred sediment transport processes in the Alías-Almanzora canyon system (SW Mediterranean): On the role of the sediment supply. Marine Geology 393, 21-34.

Reeder, D.B., Ma, B.B., Yang, Y.J., 2011. Very large subaqueous sand dunes on the upper continental slope in the South China Sea generated by episodic, shoaling deep-water internal solitary waves. Marine Geology 279, 12-18.

Reijenstein, H.M., Posamentier, H.W., Bhattacharya, J.P., 2011. Seismic geomorphology and high-resolution seismic stratigraphy of inner-shelf fluvial, estuarine, deltaic, and marine sequences, Gulf of Thailand. AAPG Bulletin 95, 1959-1990.

Richards, M., Bowman, M., Reading, H., 1998. Submarine-fan systems I: characterization and stratigraphic prediction. Marine and Petroleum Geology 15, 689-717.

Slootman, A., Cartigny, M.J.B., 2020. Cyclic steps: Review and aggradation-based classification. Earth-Science Reviews 201, 102949.

Smith, D.P., Ruiz, G., Kvitek, R., Iampieto, P.J., 2005. Semiannual patterns of erosion and deposition in upper Monterey Canyon from serial multibeam bathymetry. GSA Bulletin 117, 1123-1133.

Stow, D.A.V., Hernández-Molina, F.J., Llave, E., Sayago-Gil, M., del Río, V.D., Branson, A., 2009. Bedform-velocity matrix: The estimation of bottom current velocity from bedform observations. Geology 37, 327-330.

Symons, W.O., Sumner, E.J., Talling, P.J., Cartigny, M.J.B., Clare, M.A., 2016. Large-scale sediment waves and scours on the modern seafloor and their implications for the prevalence of supercritical flows. Marine Geology 371, 130-148.

Talling, P.J., Allin, J., Armitage, D.A., Arnott, R.W.C., Cartigny, M.J.B., Clare, M.A., Felletti, F., Covault, J.A., Girardclos, S., Hansen, E., Hill, P.R., Hiscott, R.N., Hogg, A.J., Clarke, J.H., Jobe, Z.R., Malgesini, G., Mozzato, A., Naruse, H., Parkinson, S., Peel, F.J., Piper, D.J.W., Pope, E., Postma, G., Rowley, P., Sguazzini, A., Stevenson, C.J., Sumner, E.J., Sylvester, Z., Watts, C., Xu, J.P., 2015. Key future directions for research on turbidity currents and their deposits. Journal of Sedimentary Research 85, 153-169.

Wang, W.J., 2000. Propagation of tidal waves and development of sea-bottom sand ridges and sand ripples in northern South China Sea. Tropic Oceanology 19, 1-7 (in Chinese with English Abstract).

Wang, X.X., Wang, Y.M., He, M., Chen, W., Zhuo, H.T., Gao, S.M., Wang, M.H., Zhou, J.W., 2017. Genesis and evolution of the mass transport deposits in the middle segment of the Pearl River canyon, South China Sea: insights from 3D seismic data. Marine and Petroleum Geology 88, 555-574.

Wang, X.X., Zhuo, H.T., Wang, Y.M., Mao, P.X., He, M., Chen, W.T., Zhou, J.W., Gao, S.M., Wang, M.H., 2018. Controls of contour currents on intra-canyon mixed sedimentary processes: Insights from the Pearl River Canyon, northern South China Sea. Marine Geology 406, 193-213.

Weimer, P., Slatt, R.M., 2007. Deepwater-reservoir elements: channels and their sedimentary fill. In:

Weimer, P., Slatt, R.M. (Eds.), Introduction to the petroleum geology of deepwater settings. AAPG studies in Geology 57, 171-276.

West, L.M., Perillo, M.M., Olariu, C., Steel, R.J., 2019. Multi-event organization of deepwater sediments into bedforms: Long-lived, large-scale antidunes preserved in deepwater slopes. Geology 47, 391-394.

Wu, L.Y., Xiong, X.J., Li, X.L., Shi, M.C., Guo, Y.Q., Chen, L., 2016. Bottom currents observed in and around a submarine valley on the continental slope of the northern South China Sea. Journal of Ocean University of China (Oceanic and Coastal Sea Research) 15, 947-957.

Wynn, R.B., Masson, D.G., Stow, D.A.W., Weaver, P.P.E., 2000a. Turbidity current sediment waves on the submarine slopes of the western Canary Islands. Marine Geology 163, 185-198.

Wynn, R.B., Weaver, P.P.E., Ercilla, G., Stow, D.A.V., Masson, D.G., 2000b. Sedimentary processes in the Selvage sediment-wave field, NE Atlantic: new insights into the formation of sediment waves by turbidity currents. Sedimentology 47, 1181-1197.

Wynn, R.B., Stow, D.A.V., 2002. Classification and characterization of deep-water sediment waves. Marine Geology 192, 7-22.

Wynn, R.B., Piper, D.J., Gee, M.J., 2002. Generation and migration of coarse-grained sediment waves in turbidity current channels and channel-lobe transition zones. Marine Geology 192, 59-78.

Wynn, R.B., Masson, D.G., 2008. Sediment waves and bedforms. In: Rebesco, M., and Camerlenghi, A. (Eds.), Contourites, Developments in Sedimentology, vol. 60. Elsevier, Amsterdam, pp. 289-300.

Xu, J.P., Wong, F.L., Kvitek, R., Smith, D.P., Paull, C.K., 2008. Sandwave migration in Monterey submarine canyon, central California. Marine Geology 248, 193-212.

Zhang, G.C., Yang, H.Z., Chen, Y., Ji, M., Wang, K., Yang, D.S., Han, Y.X., Sun, Y.H., 2014. The Baiyun

Sag: a giant rich gas-generation sag in the deepwater area of the Pearl River Mouth Basin. Natural Gas Industry 34 (11), 11-25 (in Chinese with English abstract).

Zhong, G.F., Cartigny, M.J.B., Kuang, Z.G., Wang, L.L., 2015. Cyclic steps along the South Taiwan Shoal and West Penghu submarine canyons on the northeastern continental slope of the South China Sea. GSA Bulletin 127, 804-824.

Zhou, W., Wang, Y.M., Gao, X.Z., Zhu, W.L., Xu, Q., Xu, S., Cao, J.Z., Wu, J., 2015. Architecture, evolution history and controlling factors of the Baiyun submarine canyon system from the middle Miocene to Quaternary in the Pearl River Mouth Basin, northern South China Sea. Marine and Petroleum Geology 67, 389-407.

Zhu, M.Z., Graham, S., Pang, X., McHargue, T., 2010. Characteristics of migrating submarine canyons from the middle Miocene to present: implications for paleoceanographic circulation, northern South China Sea. Mar. Pet. Geol. 27, 307-319.

Zhuo, H.T., Wang, Y.M., Shi, H.S., He, M., Chen, W.T., Li, H., Wang, Y., Yan, W.Y., 2015. Contrasting fluvial styles across the mid-Pleistocene climate transition in the northern Shelf of the South China Sea: Evidence from 3D seismic data. Quaternary Science Reviews 129, 128-146.

Figure captions:

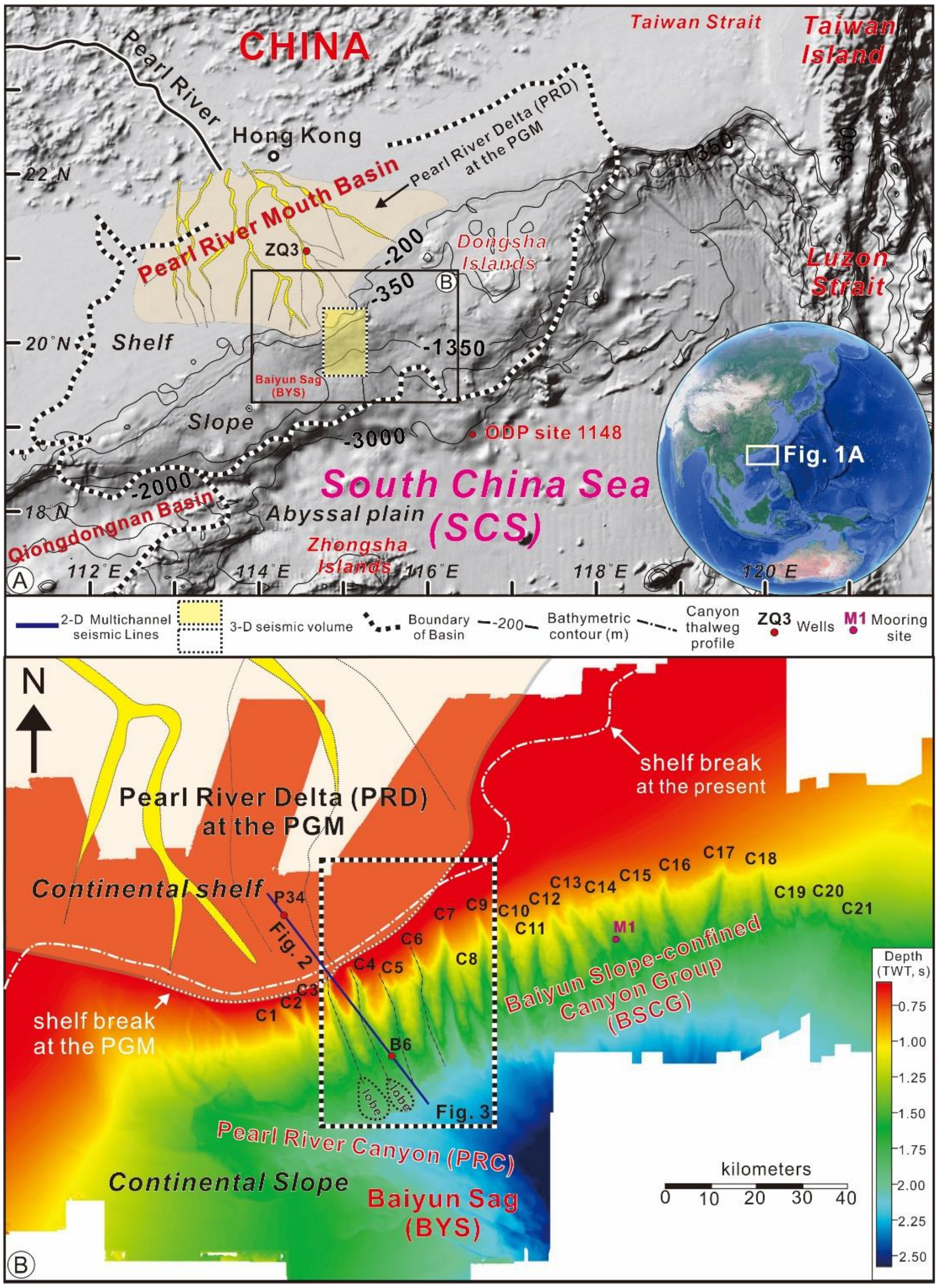

Figure 1. (A) Map showing the geological barckground and the location of the study area along the northern South China Sea (SCS) margin. The study area is located in the Baiyun Sag (BYS), a deep-water slope sub-basin of the Pearl River Mouth Basin (PRMB). At the Penultimate Glacial Maximum (PGM), the Pearl River Delta (PRD) was a shelf-margin delta fed by the Pearl River (after Lüdmann et al., 2001). Locations of well ZQ3 and the ODP site 1148 are labeled. Index map showing the location of Fig. 1A in *Google Earth*™. (B) Bathymetric map in two-way traveltime (TWT) of the modern seafloor. Labels indicate the PRD, shelf breaks (at PGM and present), slope-confined canyons (C1-C21), canyon thalweg profiles (C3-C6), terminal lobes, and the mooring site (site M1) in C14 (Wu et al., 2016). Locations of the seismic reflection data (2-D profiles and 3-D volume) as well as wells P34 and B6 are also labeled.

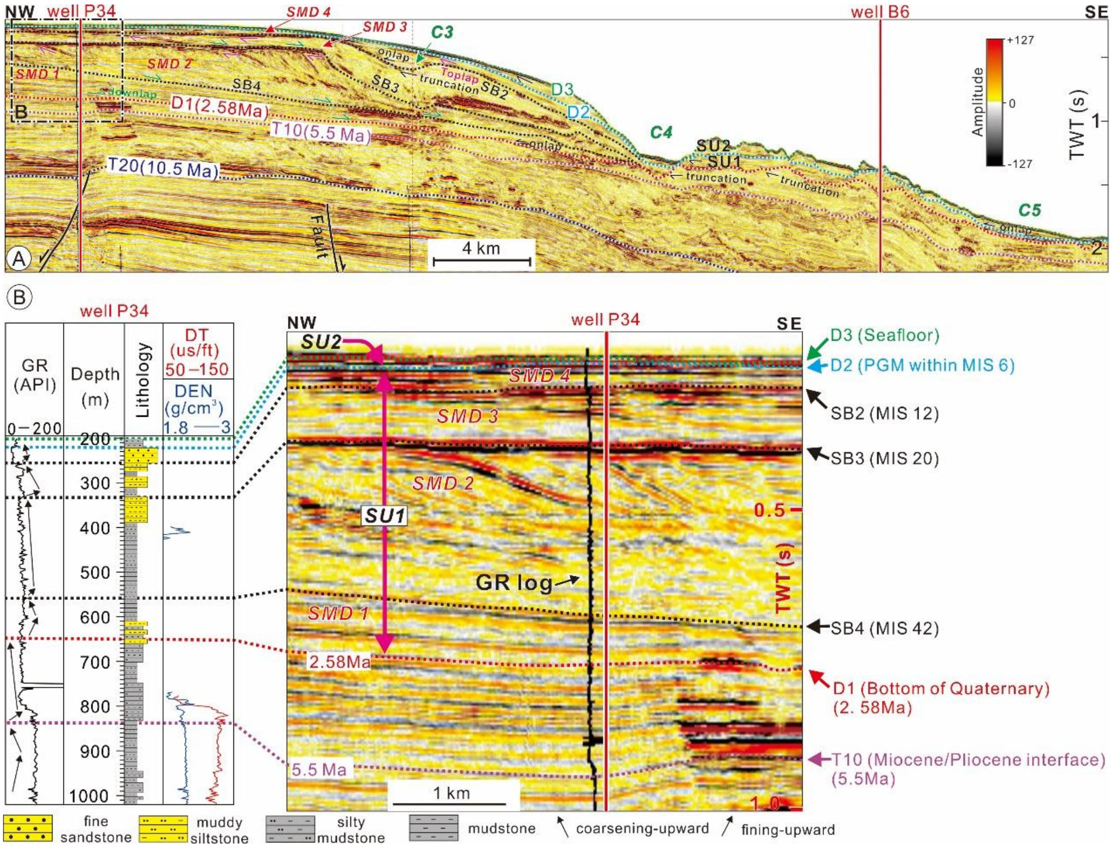

Figure 2. (A) Two-dimensional (2-D) multichannel seismic reflection profile through wells P34, B6 and submarine canyons (C3, C4 and C5) showing the seismic stratigraphic framework of the interpreted Late Miocene-Quaternary shallow sedimentary record (10.5 Ma-present). The layer of interest in this study is the Quaternary sedimentary record that can be divided into two seismic units (SU1 and SU2) bounded by discontinuities D1, D2 and D3. Note that four phases of the Pearl River shelf-margin delta (SMD1-4) were developed at the shelf edge in SU1. Locations of the profile and wells are shown in Fig. 1. (B) Seismic-well tie analysis based on well P34 illustrating the calibration between discontinuities T10-D3 and the corresponding marine isotope stages (MIS) from wells P34 and ZQ3 (Feng et al., 1996; Zhuo et al., 2015; Liu et al., 2019).

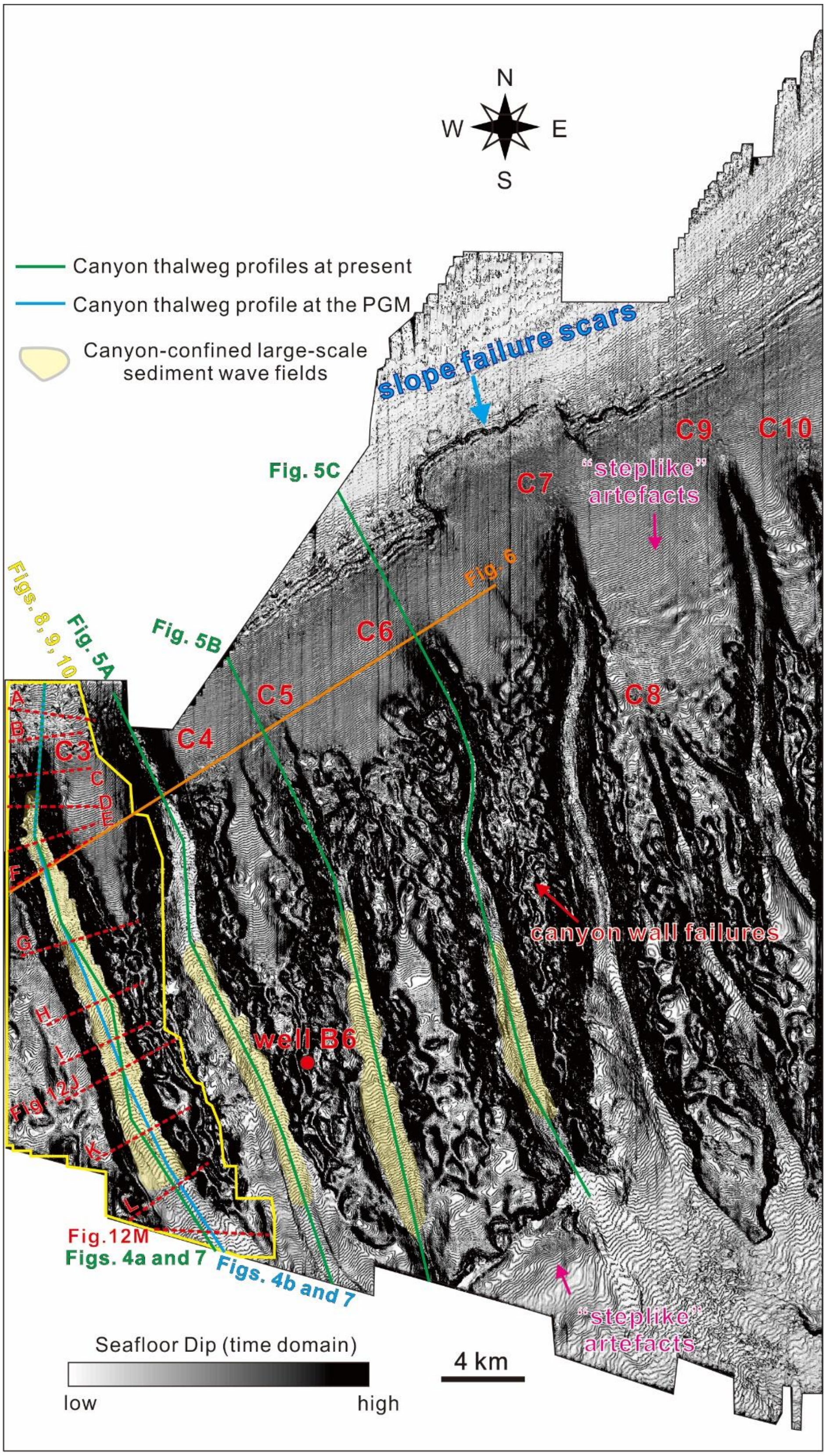

Figure 3. Seafloor dip map showing the distribution of canyon-confined large-scale sediment wave fields, modern submarine slope-confined canyons (C3-C10), as well as the location of seismic profiles and the area analyzed in this study. Note the abundant "steplike" artefacts on the seafloor dip map. Location is shown in Fig. 1.

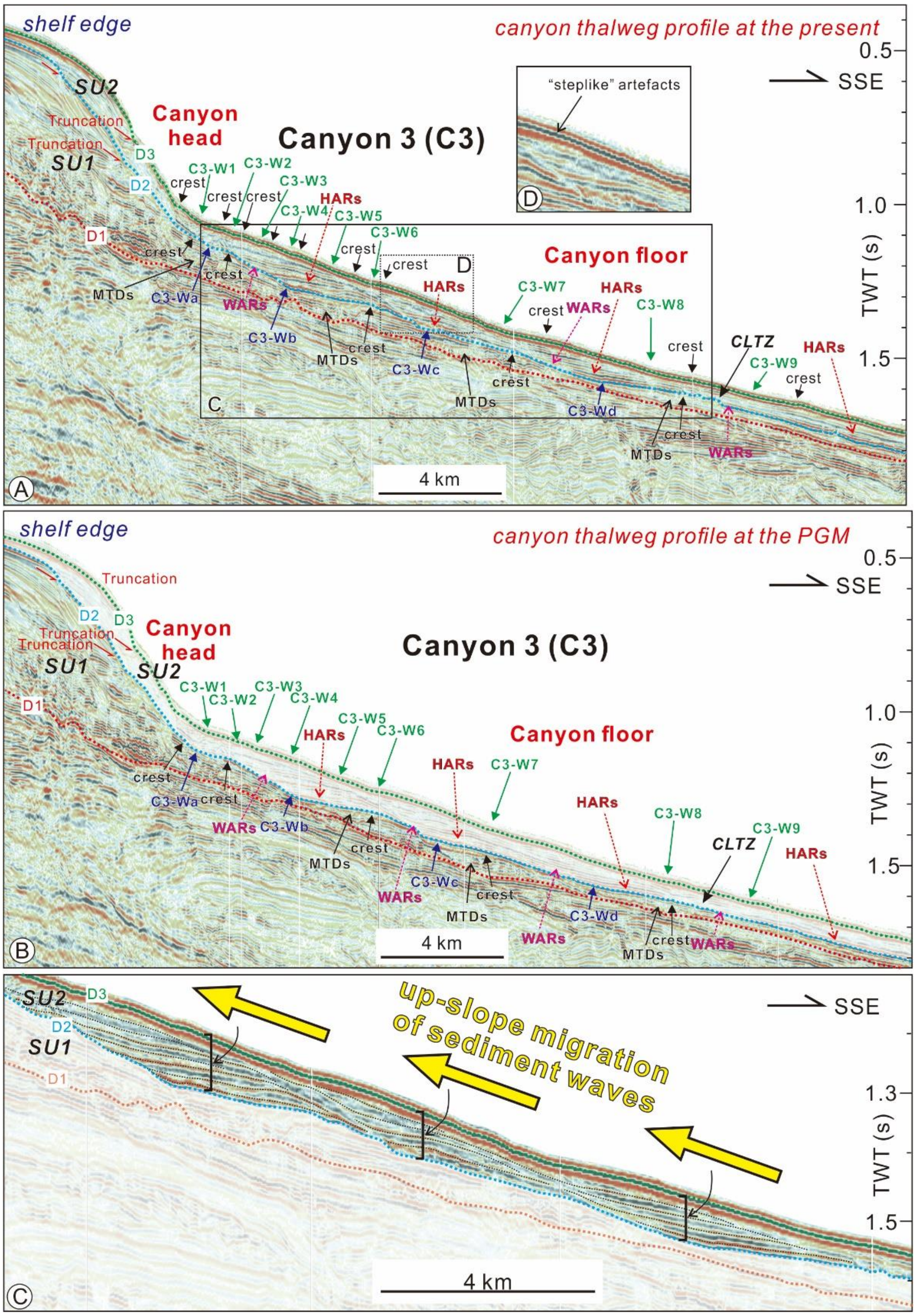

Figure 4. Canyon thalweg profiles along the present and ancient C3 canyon axes. (A) Along the present canyon axis, (B) Along the canyon axis at the PGM**.** Four large-scale sediment waves (C3-W*a-d*) along discontinuity D2 (PGM≈140 ka) and nine large-scale sediment waves (C3-W*1-9*) along discontinuity D3 (modern seabed) were identified. These sediment waves show an up-slope migrating feature in seismic unit SU2. (C) Local enlarged profile showing the distinct up-slope migrating feature of the large-scale sediment waves along the canyon thalweg. (D) The "steplike" artefacts on the seabed. HARs=High amplitude reflections. WARs=Weak amplitude reflections. MTDs=Mass transport deposits. CLTZ=canyon/channel-lobe transition zone. Locations of profiles are shown in Fig. 3.

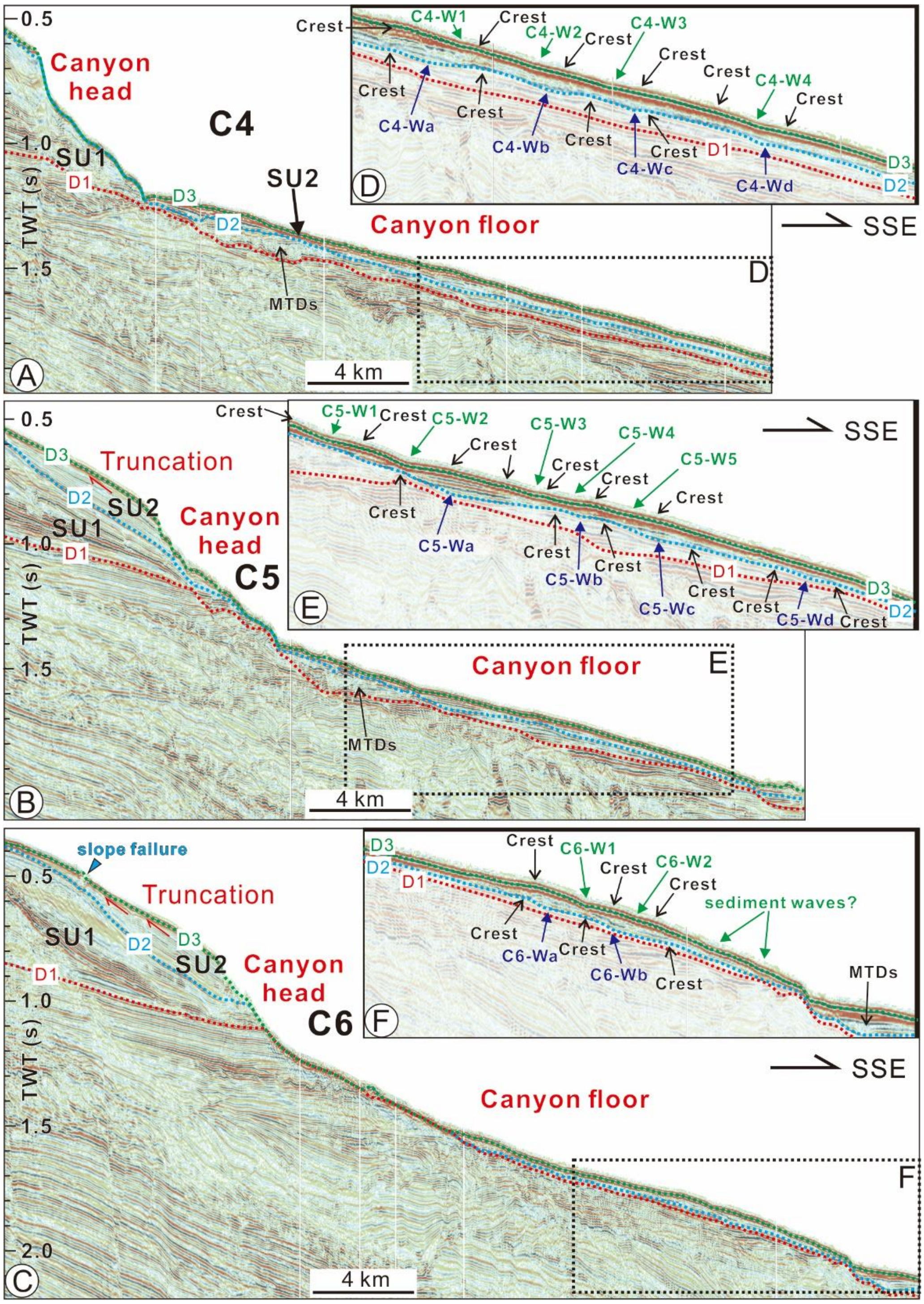

Figure 5. (A)-(C) Seismic profiles along the present thalwegs of C4, C5 and C6 with interpreted discontinuities D1-D3, seismic units SU1 and SU2, and large-scale sediment waves. Note that the heads of these canyons are all blind on the upslope and do not erode the continental shelf. Locations of these profiles are shown in Fig. 3. (D)-(F) Enlarged profiles showing the large-scale sediment waves along D2 and D3. A total of ten large-scale sediment waves (C4-W*a-d*, C5-W*a-d*, C6-W*a-b*) and eleven large-scale sediment waves (C4-W*1-4*, C5-W*1-5*, C6-W*1-2*) were identified along discontinuities D2 and D3, respectively. Also note the mass-transport deposits (MTD) developed in SU1.

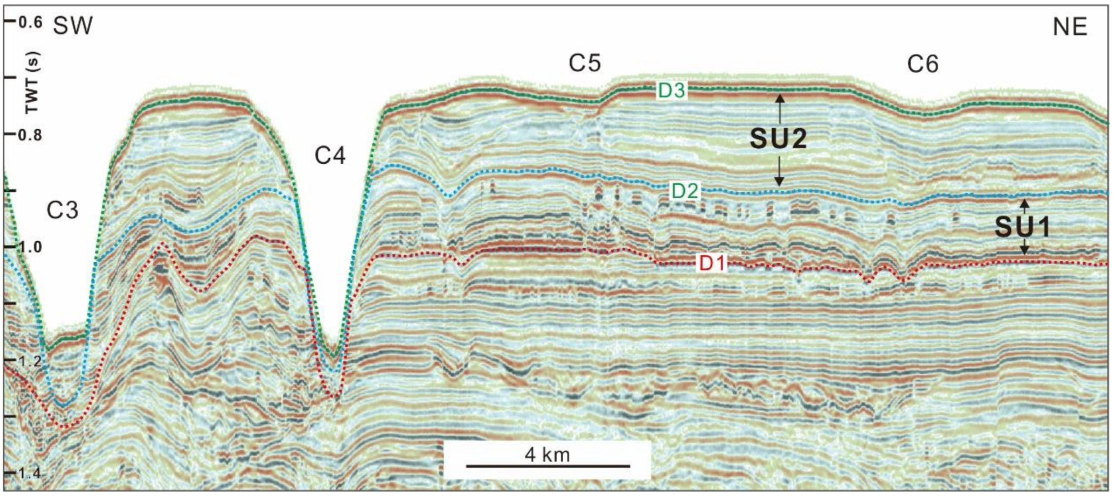

Figure 6. Alongslope seismic reflection profile across the heads of submarine canyons C5 and C6 showing that C3 and C4 erode the seafloor farther upstream than C5 and C6 at the D1, D2, D3 interfaces. The location is shown in Fig. 3.

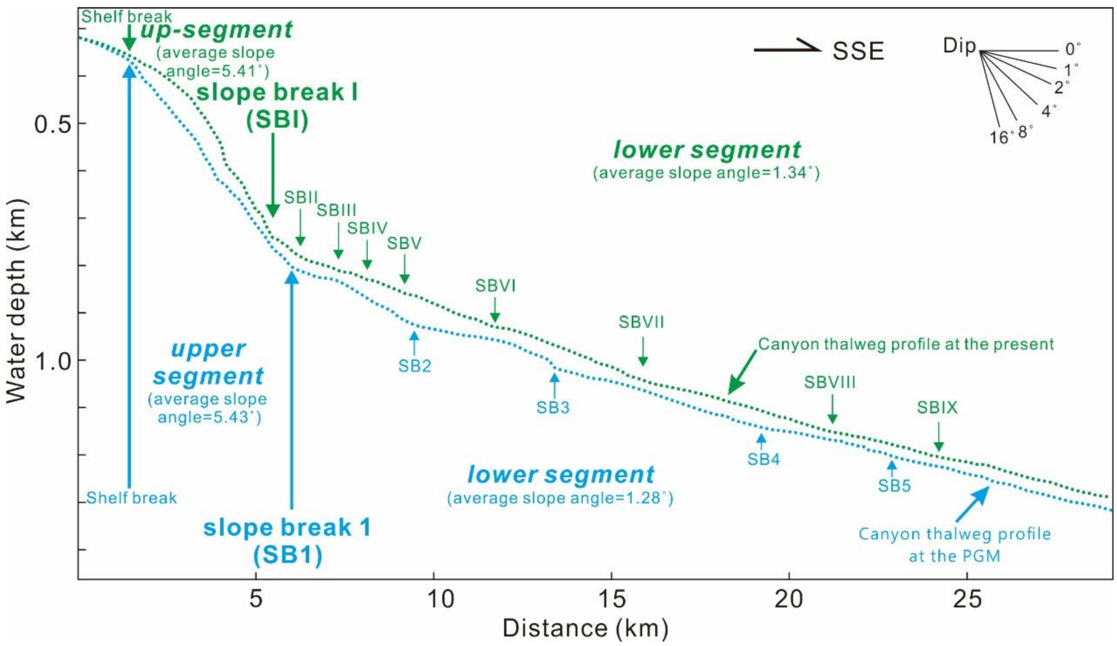

Figure 7. Longitudinal bathymetric profiles showing morphological characteristics of the thalwegs within canyon 3 (C3) at the PGM (light blue dotted line) and present (green dotted line). Five slope breaks (SB1-SB5) along the PGM thalweg and nine slope breaks (SBI-SBIX) along the present thalweg have been identified. The longitudinal canyon thalweg profiles at the PGM and the present can be both divided into two segments (upper and lower) with different average slope gradients separated by SB1 and SBI, respectively. Overall, the longitudinal slope gradient of lower segment of the canyon thalweg was gentler at the PGM than that at the present. The location is shown in Fig. 3.

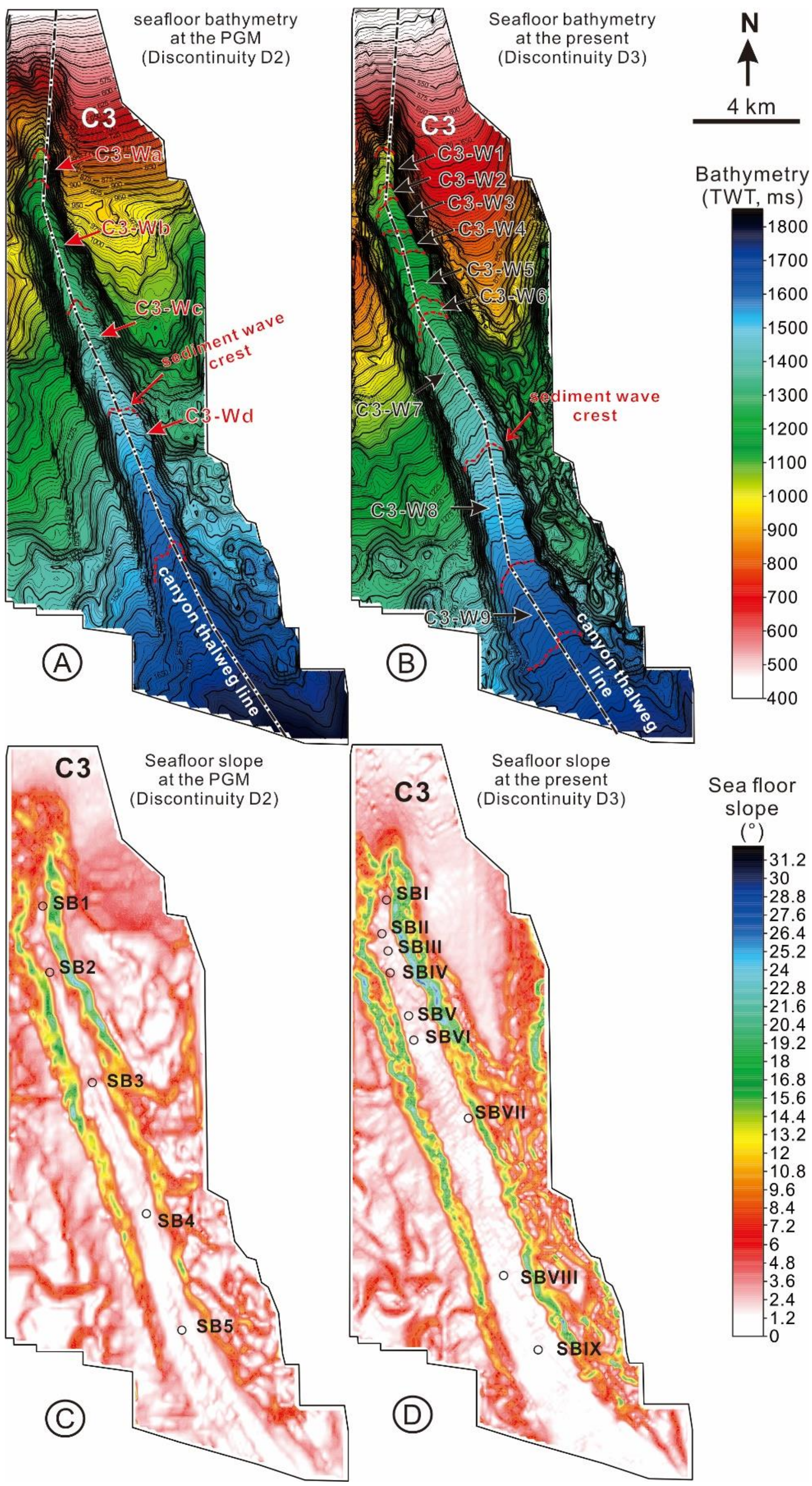

Figure 8. (A) and (B) Bathymetric maps of the canyon C3 in two-way-traveltime (TWT) respectively at the PGM and at the present. Four canyon-confined large-scale sediment waves (C3-W*a-d*) with their wave crests at the PGM and nine canyon-confined large-scale sediment waves (C3-W*1-9*) with their wave crests are identified at the present are identified. (C) and (D) Sea floor slope maps of the canyon C3 respectively at the PGM and at the present. Five (SB*1-5*) along the thalwag of C3 at the PGM and nine (SB*I-IX*) slope breaks along the thalwag of C3 at the present are labeled.

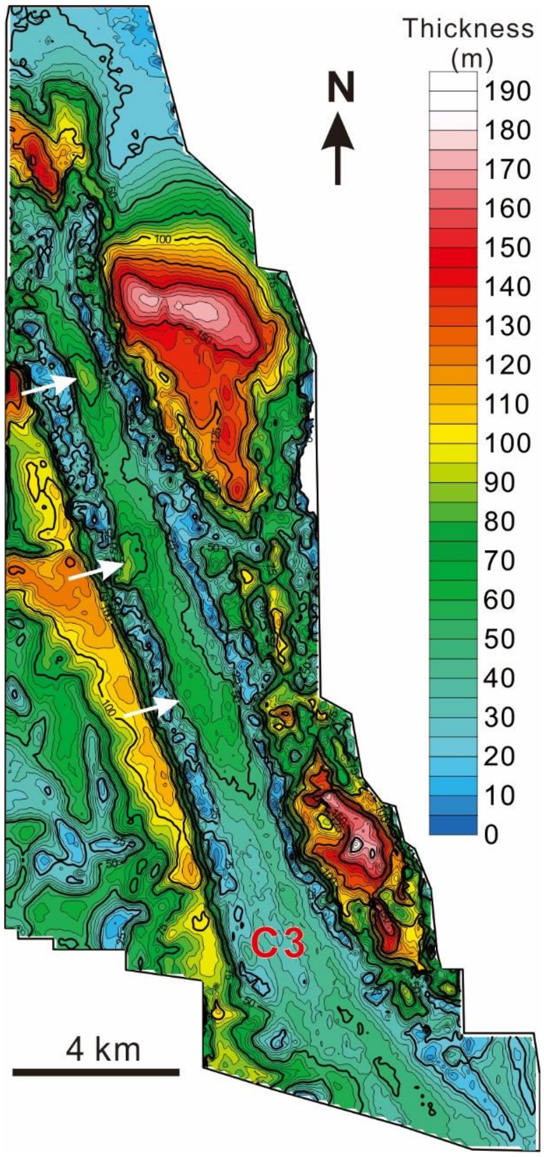

Figure 9. Isochore map in meters of SU2 covering the development area of canyon C3 showing the distribution of depocenters (marked with white arrows) associated with large-scale sediment waves in the thalweg of C3 in SU2. The location is shown in Fig. 3.

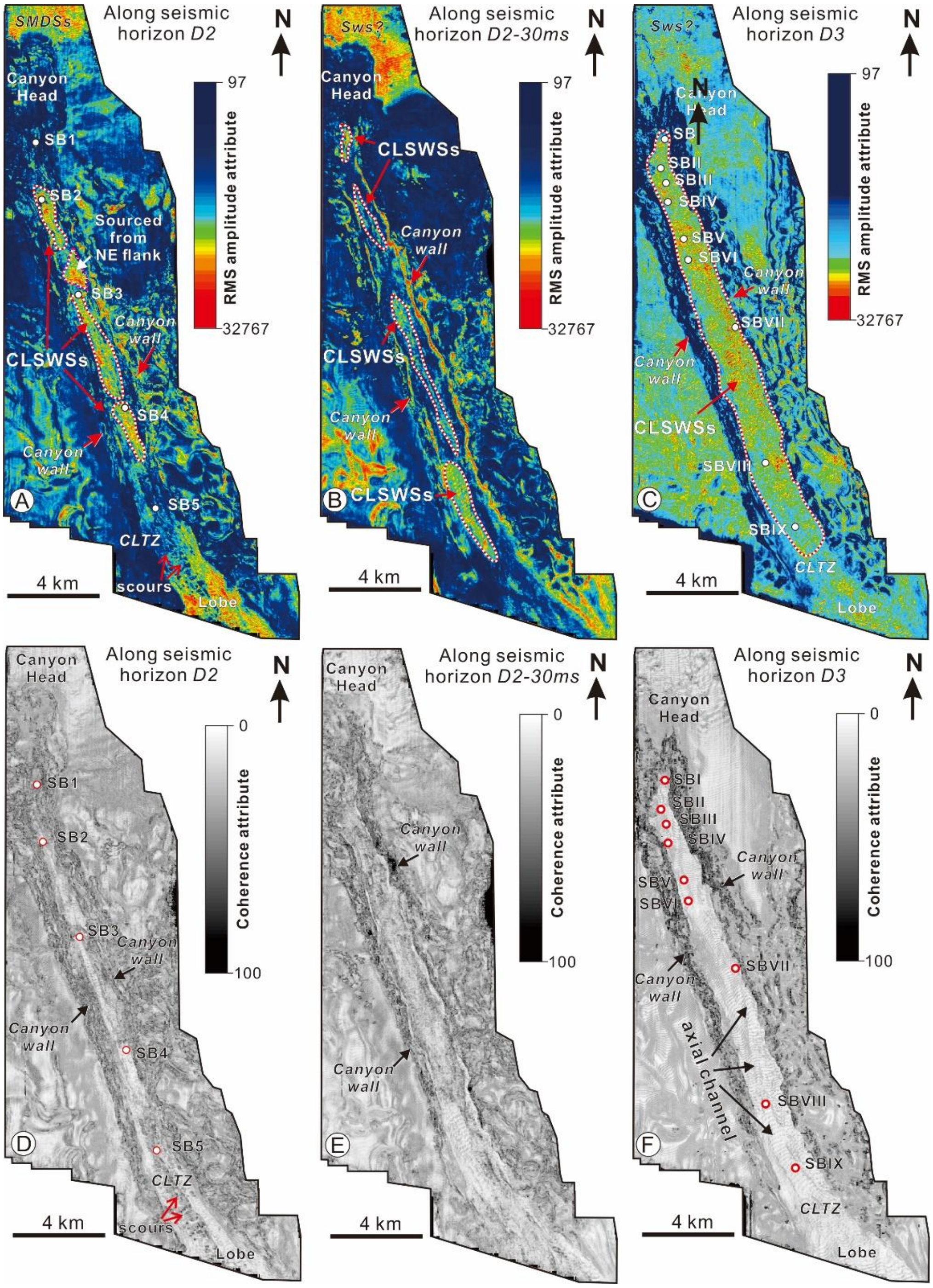

Figure 10. Seismic attribute maps of canyon 3 (C3) predicting the distribution of sands in and around the canyon. See Figure 3 for location. (A)-(C) *RMS amplitude* and (D)-(E) *coherence* attributes calculated along seismic horizon D2 (seabed at the PGM), D2-30 ms (within SU2), and seismic horizon D1 (modern seabed), respectively. Canyon-confined large-scale sediment wave related sands (CLSWSs), lobes, shallow water shelf-margin delta sands (SMDSs) and possible shelf-edge sandwaves (SWs) are shown to have attributes of high RMS amplitude with low coherence. SB*1-5* and SB*I-IX* are also labeled, as in Figure 7. At the PGM, the canyon head cut onto the shelf and linked with the SMDSs. At the present, the canyon head blinds on the upper slope and links with the SWs. Both at the PGM and present, the channel-lobe transition zone (CLTZ) and the terminal lobe have developed at the downstream end of the canyon. In addition, axial channel can be found in the present canyon thalweg.

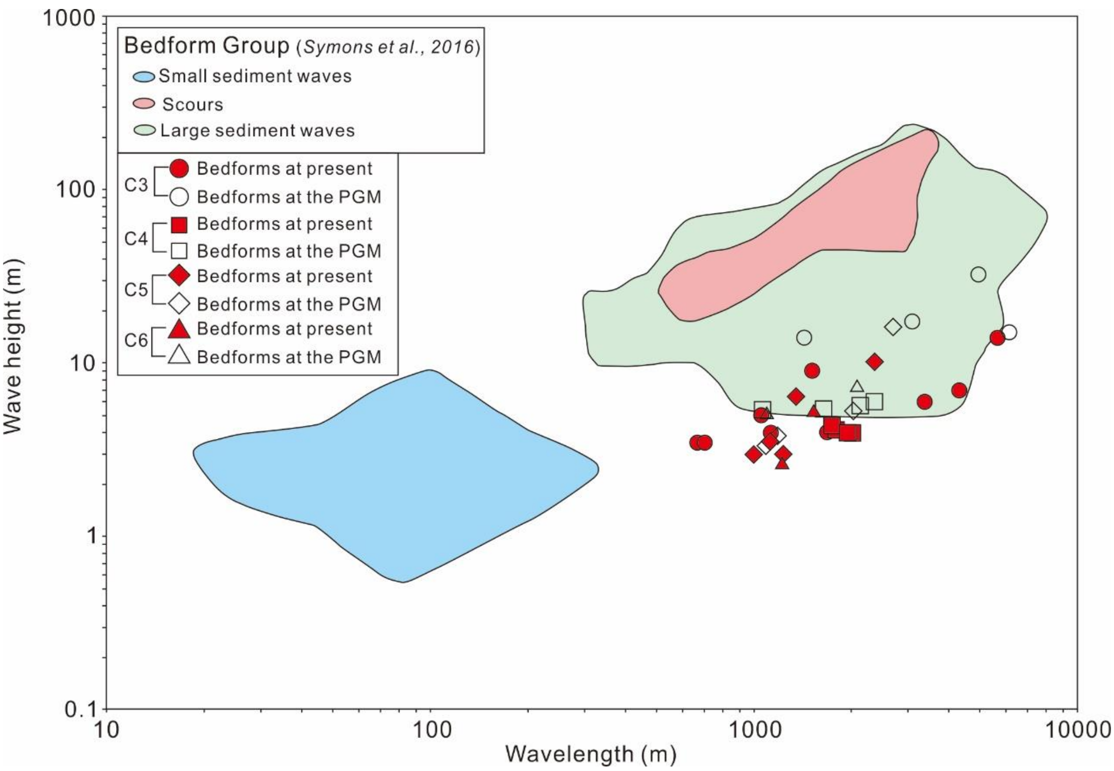

Figure 11. Logarithmic plot of wavelength versus wave height of the wave-like bedforms in this study compared to Symons et al. (2016). The data points are shown in Table 1.

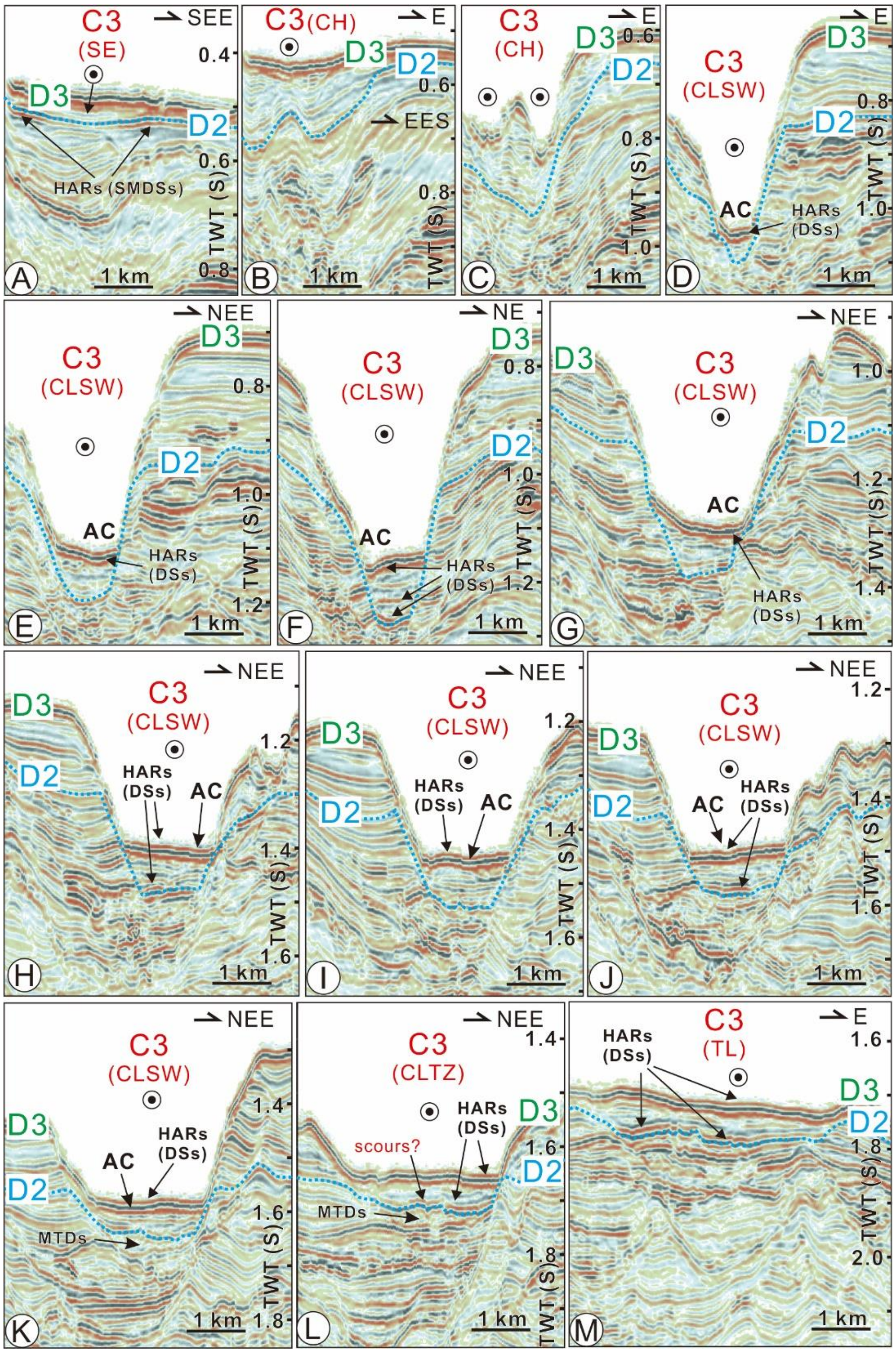

Figure 12. Transverse seismic profiles across C3 showing the morphological changes and infills of the canyon along the downstream direction. Locations are shown in Fig. 3. (A) Cross section along the shelf-edge (SE). It shows the paleo-C3 head incising the shelf-edge and linking with the shelf-margin delta sands (SMDSs) characterized by high-amplitude reflections (HARs) on seismic horizon D2. The modern canyon does not incise the shelf. (B)-(C) Cross sections at the canyon head (CH). The canyon is shown in a V-shaped cross-sectional pattern. (D)-(K) Cross sections cut through the canyon-confined large-scale sediment waves (CLSWs). (L)-(M) At the downstream, the canyon changes into a terminal lobe (TL) through the channel-lobe transition zone (CLTZ). Note the deepwater sands (DSs) in the canyon thalweg shown by HARs. Also note the development of the axial channel (AC) in the modern canyon.

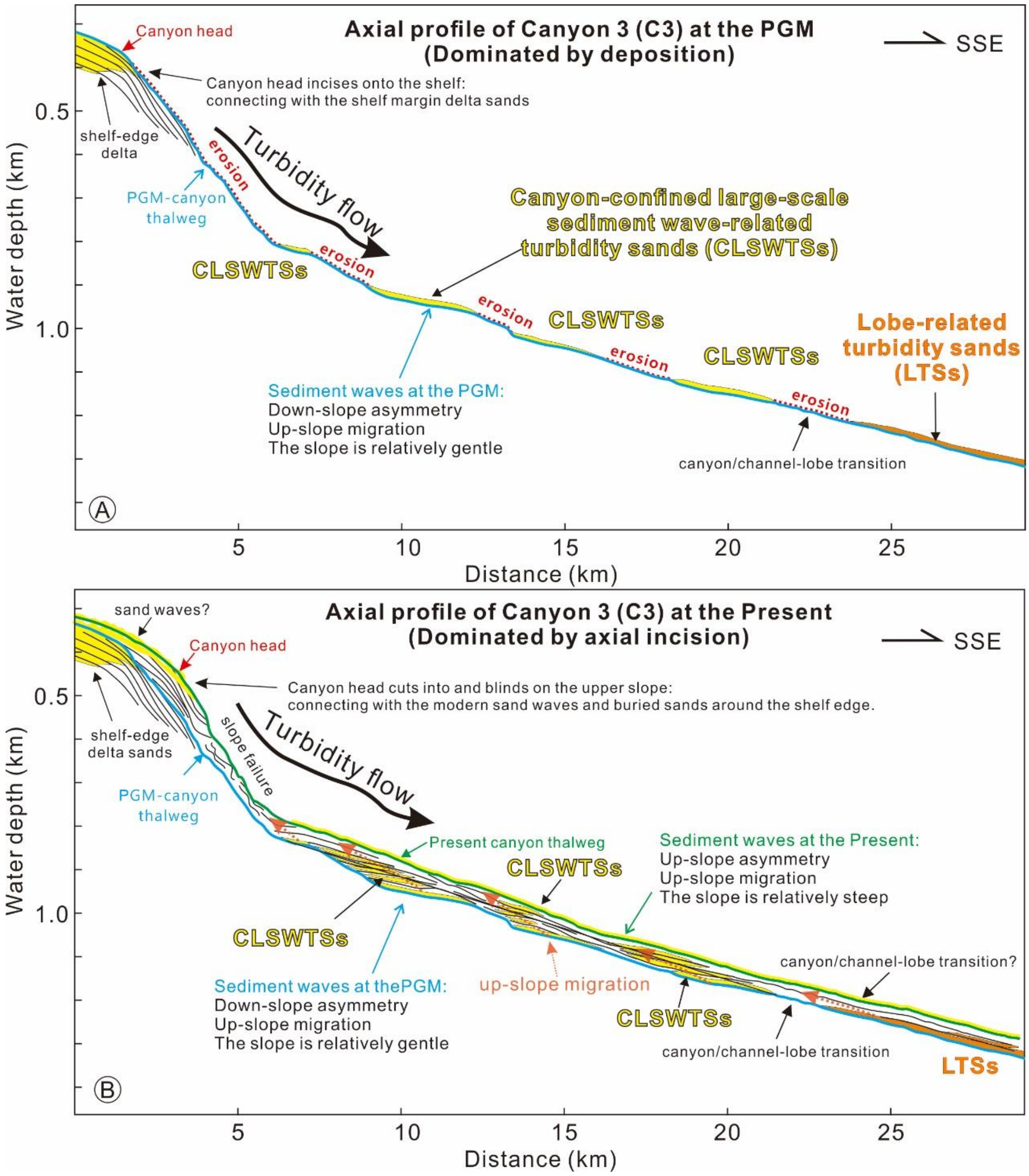

Figure 13. The coevolution of the canyon and its confined large-scale sediment waves. (A) As the sea level dropped below the shelf edge at the PGM, the large-scale sediment waves developed along the canyon thalweg. The shelf-margin delta fed abundant coarse-grained sediments into the canyon head, forming supercritical turbidity currents that flow down the relatively gentle (but still steep) canyon thalweg, forming up-slope migrating down-slope asymmetrical partially depositional cyclic steps. The deep-water sands were deposited mainly on the stoss sides of the cyclic steps, while their lee sides were dominated by erosion. (B) After the PGM, the Baiyun Sag was dominated by the development of the slope-confined canyon system due to the high sea level and the retrograding of the Pearl River sediment supply. The two-dimensional (2-D) morphology of the large-scale sediment waves (i.e., cyclic steps) transformed into the up-slope asymmetry from the down-slope asymmetry due to stronger supercritical turbidity flows flowing through an overall steeper slope compared to the PGM period, with the result that the axial incision is dominated along the canyon thalweg at present.

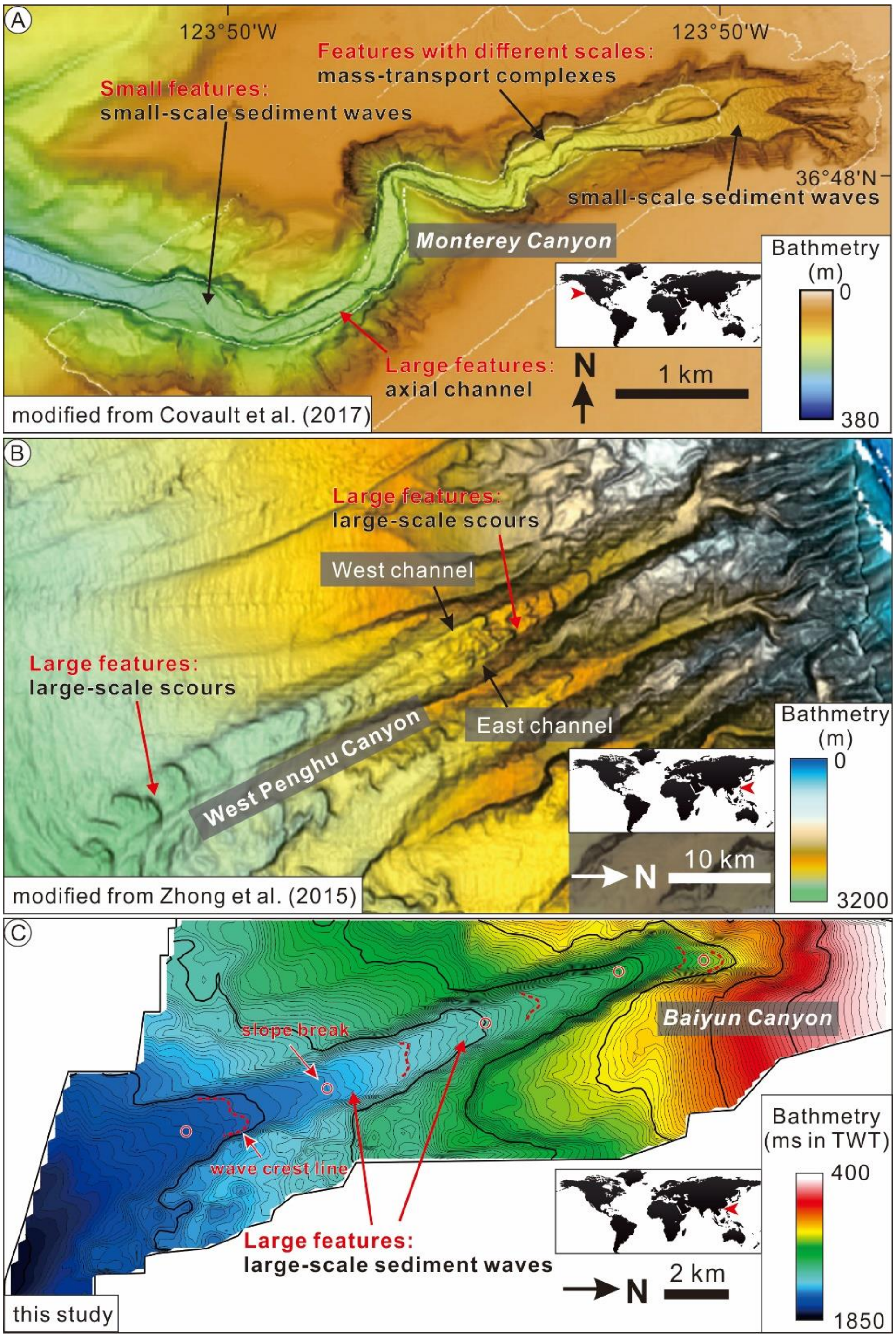

Figure 14. Comparison of morphological features on the floors of the Monterey Canyon, the West Penghu Canyon and the Baiyun Canyon. (A) Monterey Canyon, offshore central California (Covault et al., 2017). It shows that both small features (e.g., small-scale sediment waves and mass-transport complexes) and large features (e.g., the axial channel and large-scale mass-transport complexes) are developed on the canyon floor. (B) West Penghu Canyon, northeastern continental slope of the South China Sea (Zhong et al., 2015). It shows that large features (e.g., large-scale scours) are developed on the canyon floor. (C) Baiyun Canyon, offshore Hongkong (representative canyon C3 at the PGM in this study). It shows that large-scale sediment waves (large features) can also be developed on the canyon floor.

Table 1. Collection of 2-D sediment wave geometries[1] measured from 3-D seismic data

Canyon	Time	Wave number	Wavelength (km)	Wave height (m)	Lee side slope (°)	Stoss side slope (°)	Sediment wave slope (°)	2-D morphology
C3	Present	C3-W1	1.509	9.0	3.00	1.54	2.24	Up-slope asymmetry
		C3-W2	0.696	3.5	1.73	0.74	1.23	Up-slope asymmetry
		C3-W3	0.667	3.5	1.91	0.74	1.50	Up-slope asymmetry
		C3-W4	1.131	4.0	1.84	0.79	1.57	Up-slope asymmetry
		C3-W5	1.683	4.0	1.92	1.30	1.69	Up-slope asymmetry
		C3-W6	1.044	5.0	1.97	0.75	1.26	Up-slope asymmetry
		C3-W7	5.628	14.0	1.64	0.95	1.44	Up-slope asymmetry
		C3-W8	4.293	7.0	1.28	0.81	1.15	Up-slope asymmetry
		C3-W9	3.364	6.0	1.15	0.72	0.96	Up-slope asymmetry
	PGM	C3-Wa	1.422	14.0	4.27	1.17	1.93	Down-slope asymmetry
		C3-Wb	4.903	32.5	2.50	0.86	1.55	Down-slope asymmetry
		C3-Wc	3.075	17.5	2.36	1.02	1.54	Down-slope asymmetry
		C3-Wd	6.090	15.0	1.40	0.81	1.12	Down-slope asymmetry
C4	Present	C4-W1	1.959	4.0	1.37	0.84	1.26	Up-slope asymmetry
		C4-W2	2.016	4.0	1.40	0.79	1.25	Up-slope asymmetry
		C4-W3	1.781	4.2	1.30	0.68	1.12	Up-slope asymmetry
		C4-W4	1.734	4.4	1.50	0.86	1.25	Up-slope asymmetry
	PGM	C4-Wa	2.125	5.7	1.23	0.66	0.92	Down-slope asymmetry
		C4-Wb	2.335	6.0	1.21	0.51	1.01	Up-slope asymmetry
		C4-Wc	1.628	5.4	1.36	0.14	1.05	Up-slope asymmetry
		C4-Wd	1.059	5.3	1.70	0.49	1.30	Up-slope asymmetry
C5	Present	C5-W1	1.351	6.4	2.03	0.83	1.51	Up-slope asymmetry
		C5-W2	2.353	10.1	1.69	0.72	1.25	Up-slope asymmetry
		C5-W3	1.005	3.0	1.37	0.55	1.10	Up-slope asymmetry
		C5-W4	1.121	3.5	1.25	0.44	0.88	Up-slope asymmetry
		C5-W5	1.228	3.0	1.29	0.59	1.10	Up-slope asymmetry
	PGM	C5-Wa	2.694	16.2	1.97	0.58	1.23	Down-slope asymmetry
		C5-Wb	1.176	3.8	1.14	0.06	0.89	Up-slope asymmetry
		C5-Wc	2.027	5.3	1.60	0.98	1.35	Up-slope asymmetry
		C5-Wd	1.095	3.3	1.48	0.91	1.17	Down-slope asymmetry
C6	Present	C6-W1	1.534	5.3	1.73	0.55	1.49	Up-slope asymmetry
		C6-W2	1.218	2.7	1.52	0.63	1.32	Up-slope asymmetry
	PGM	C6-Wa	1.099	5.2	2.14	0.95	1.36	Down-slope asymmetry
		C6-Wb	2.086	7.4	1.98	1.07	1.37	Down-slope asymmetry

[1] Geometric parameters for describing the 2-D sediment wave listed in this table are referenced from Cartigny et al. (2011).